2. 方法

2.1. 手順の概要

今回開発した新規 *de novo* 分子デザイン法である PMP 法の手順を図 1 に示す。まず初めに、反応原子団を有する擬似分子プローブをタンパク質の結合部位内の適切な位置にドッキングシミュレーションにより配置する。リンカーに用いる化学構造の可能な立体配座は、予め配座解析により発生しておく。仮想分子は、擬似分子プローブとリンカーを両者の特定の非水素原子位置で重ね合わせることで構築するが、それらの原子位置を結合点と呼ぶことにする。擬似分子プローブの結合点は原則として 1 箇所であるが、リンカー構造については結合点が複数存在する場合もある。そこで、可能な配置を網羅的に探索し、擬似分子プローブとリンカーの結合点を結合した仮想分子を全て作成する。最終的に、タンパク質の結合部位で仮想分子の構造最適化を行うことにより、タンパク質との結合性が高い仮想分子を選択する。

2.2. 擬似分子プローブの作成

標的分子に対する結合性が高い反応原子団の結合部位における適切な配置を探索するために、擬似分子プローブという新しいコンセプトを本研究では導入した。本研究により、*de novo* 分子デザインを実現する上で、シクロプロペニルメチル（CPM）基を反応原子団に結合させた擬似分子プローブ（図 2）を用いることが有用であると確認できた。

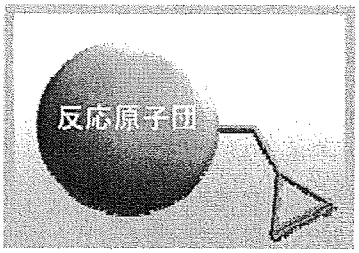

図 2 疑似分子プローブ

本アルゴリズム検証のために PDB[2]から 4 種の医薬分子とその標的分子との複合体 X 線構造を選択した。1GKC、1KE5、1OTH および 1T46 である。各構造中のリガンドとそれに基づき作成した擬似分子プローブを表 1 に示す。

PDB コード	リガンド	擬似分子プローブ
1GKC	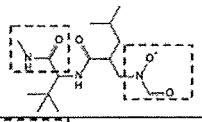	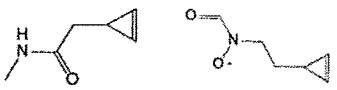
1KE5	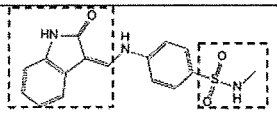	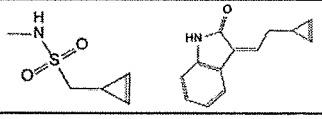
1OTH	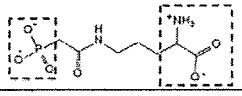	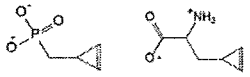
1T46	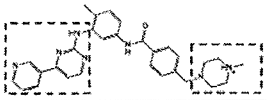	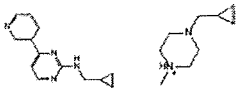

表 1 リガンドから作成した疑似分子プローブ
破線で囲んだ部分は擬似分子プローブに用いた反応原子団

2.3. 擬似分子プローブの結合部位への配置

タンパク質表面の結合部位の検出には、MOE[3] (Molecular Operating Environment) の Site Finder プログラムを用いた。Site Finder は、アルファ球と呼ばれる小球を標的分子の 4 つの重原子に接する位置に置き、そのアルファ球のクラスタ（アルファサイト）によりリガンド結合部位の形状、大きさ、親

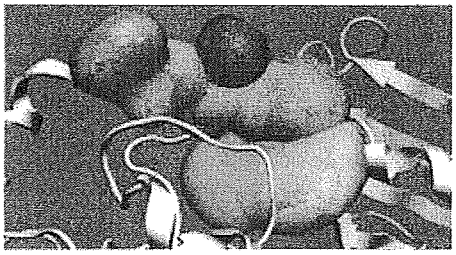
図 3 重複分割した 1OTH の結合部位

水性／疎水性領域の分布を表現する。しかし、Site Finder で求められるアルファサイトは結合部位全体を反映するため、擬似分子プローブの結合部位を求める上では必ずしも適切ではなかった。そこで本研究では、疑似分子プローブの結合部位として妥当な大きさになるように、擬似分子プローブと同程度の体積に、アルファサイトを重複分割した（図 3）。

結合部位における擬似分子プローブの結合性および結合位置はドッキング法（MOE-ASEDock[4]）により決定した。CPM 基の立体的な効果により、反応原子団はタンパク質側に配向し、CPM 基は結合部位の空洞側に配向する。即ち、CPM 基が本来のリガンドの母核構造に代わる働きをしている。実際に擬似分子プローブだけのドッキングでも、反応原子団は X 線結晶構造に近い位置に配置することができた。

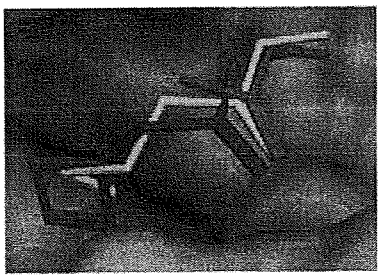

図 4 反応原子団に CPM 基または CBM 基を付加した擬似分子プローブの比較（1GKC）　赤：X 線結晶構造、緑：CPM 基を付加した擬似分子プローブ、青：CBM 基を付加した擬似分子プローブ

なお、CPM 基を持たない構造では、反応原子団の可動範囲が広くなりすぎて、X 線結晶構造とは異なる配置しか得られなかった。さらに、メチレンを除いたシクロプロペニル基や 4 員環を持つシクロブタジエニルメチル（CBM）基を用いると、それらの立体効果の影響で適切に反応原子団を配置できない場合が生じる（図 4）。

2.4. 適切なリンカー配座の検出

擬似分子プローブとリンカーを用いた仮想分子の構築は、両者の二つの非水素原子を重ね合わせることで実現した。CPM 基のメチレン炭素原子を第二結合点とし、その原子に直接結合した反応原子団の非水素原子を第一結合点とする。リンカー構造は、1 つ以上の水素原子を持つ全ての非水素原子を第一結合点とし、第一結合点から水素原子の方向へ 1.5 Å離れた点を第二結合点とした（図 5）。擬似分子プローブおよびリンカー構造の対応する第一結合点と第二結合点の重なりの誤差の許容値は、各々0.2 および 0.3 Å として、新規仮想分子を構築した。

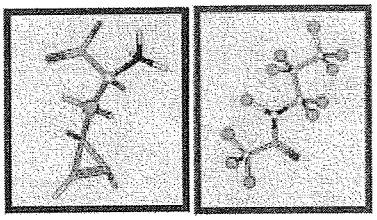

図 5 擬似分子プローブとリンカー構造の結合点　青枠：擬似分子プローブ、赤枠：リンカー構造、黄球：第一結合点、緑球：第二結合点

リンカー構造の候補構造には元のリガンド分子から反応原子団を除いた構造も考慮し、さらにその構造と同程度の体積を持つリンカー構造を DCUJ[5]から選択して、候補構造に加えた。1GKC、1KE5、1OTH および 1T46 に対して用いたリンカー構造は各々113、19、20 および 139 種類である。これらのリンカー構造の可能な立体配座は、MOE-Conformation Import 機能を用いて発生させた。擬似分子プローブに用いた反応原子団は、元のリガンド中に存在している反応原子団のみを採用した。

2.5. 構造最適化とドッキングスコア

MMFF94x 力場を用い、タンパク質の結合部位内で各仮想分子の構造最適化を行った。仮想分子の標的タンパク質分子に対する結合性は次の U_{dock} により評価した。

$$U_{dock} = U_{ele} + U_{vdw} + U_{strain}$$

ここで U_{ele} はタンパク質－仮想分子間の静電相互作用エネルギー、U_{vdw} は同 van der Waals 相互作用エネルギー、U_{strain} は仮想分子のドッキング構造とドッキング構造から最も近い極小構造のポテンシャルエネルギーの差である。

3. 結果

表 2 の「仮想分子の配座数」は、PMP 法により生成した仮想分子のドッキング構造の数である。「U_{dock} の最小値」は、ドッキング構造中の最小 U_{dock} 値を示す。得られた仮想分子の種類は、1GKC、1KE5、1OTH および 1T46 に対して各々3384、111、254 および 4519 だった。

1OTH では U_{dock} による評価が最も良好な分子が実際のリガンドであった、その構造と X 線結晶構造との RMSD（対応する非水素原子位置に関する root mean square deviation）は 1.13Å であり、この場合は PMP 法によって、良好に分子が構築できたことを示す。1GKC、1KE5 では、U_{dock} 値についてそれぞれ第 65 位および 61 位の構造が X 線結晶構造と最も近く、それらの RMSD も十分小さな値だった。一方、1T46 ではかなりの数の配座が得られたにも関わらず、今回の計算条件では X 線結晶構造と同じ分子は得られなかった。しかし、擬似分子プローブの第一結合点における一致許容範囲を今回採用した 0.2Å から 0.3Å に広げれば、この構造についても X 線結晶構造に近い仮想分子を得ることができた。しかし結合点の一致許容範囲を 0.3Å に広げることにより、多くの無意味と思われる構造が生成され、適切な仮想分子の選択が困難になった。

PDB コード	リンカー構造の数	仮想分子の配座数	U_{dock} の最小値 (kcal/mol)	X 線結晶構造に最も近い配座の U_{dock} (kcal/mol)	X 線結晶構造に最も近い配座の順位（U_{dock} 値）	X 線結晶構造との RMSD (Å)
1GKC	113	9113	-185.3	-157.8	65	1.08
1KE5	19	250	-89.38	-43.69	61	1.31
1OTH	20	989	-377.2	-377.2	1	1.13
1T46	137	11527	-107.6	-	-	-

表 2　PMP 法による計算結果

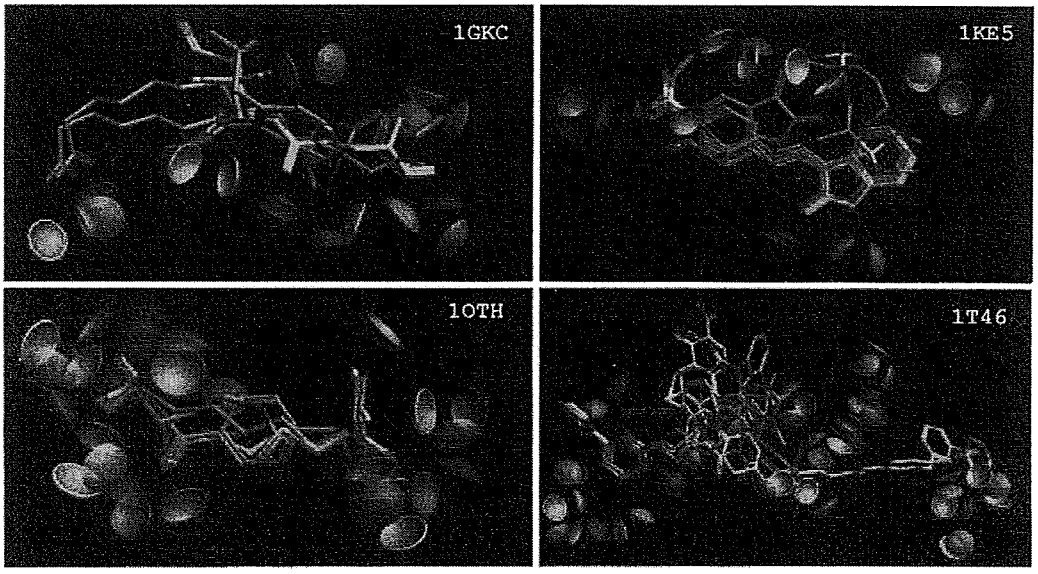

図 6　PMP 法で得られた主な化合物のドッキング構造　緑の構造は X 線結晶構造、元素で色分けした構造は PMP 法で作られた構造。紫、青の傘はそれぞれタンパク質の水素結合ドナーまたはアクセプター原子からの影響を示す。

4. 考察

新しい概念である擬似分子プローブを用いた *de novo* 分子デザイン法である PMP 法を開発し、その機能を 4 種類の標的分子に対して適用した。今回の評価では、既知のリガンドが、そのリガンドの部分化学構造を含む複数の構造断片から再構築でき、かつ標的分子の位置に X 線構造に匹敵する正確さで結合できるかどうかを検証した。一方、複合体構造中に含まれる分子が最適の

リガンドであるという保証がないので、PMP 法で得られる最良の解が X 線構造に一致することは担保されている訳ではない。また、PMP 法は、本来結合性の高い仮想分子を発生するため、これら未合成の仮想分子の中に結合性のより高いものが含まれている可能性は十分ある。しかし、今回の検証で、1OTH に関しては最終的なドッキングにより最も結合性が高いと判断された仮想分子が実際のリガンドと一致し、その配置まで正確に決定することができた。1GKC および 1KE5 でも、結合性の高い分子として得られた仮想分子の結合性上位に実際のリガンドと一致する分子が含まれていた。この 3 例を見る限り、PMP 法は十分に実用的であり、新規分子の設計を標的分子の構造のみから求める上で有用であることを示している。

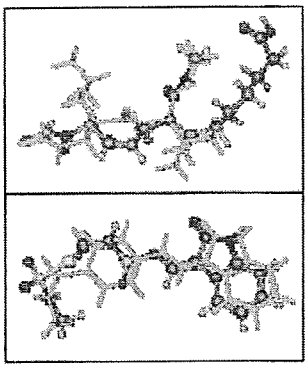

図 7　既知リガンドと異なりかつ U_{dock} がより良好な仮想分子　上段：1GKC、下段：1KE5、棒モデル：X 線結晶構造、棒球モデル：仮想分子

1T46 については今回用いたプロトコルでは、複合体中に含まれるリガンドに一致する仮想分子を生成することはできなかった。しかし、擬似分子プローブとリンカー構造の結合点の一致許容範囲を大きくすると、発生する配座数が増加するが、複合体 X 線構造中に存在するリガンド構造を発生することができた。4 分子の中で、1T46 のリガンドが最も分子サイズが大きく、かつ自由度が大きい。今回検討したプロトコルでは、この系を考慮することができなかったが、これは PMP 法の本質的な限界というより、計算条件の最適化が不十分である可能性が高く、今後 PMP 法を改良することで乗り越えることのできる課題であると考える。

水分子をプローブに用いてタンパク質表面を解析し、他分子との相互作用に関与する部位を探索することは広く行われている。そうした例には、溶媒露出表面とエピトープ性の相関解析などがある。本研究で新しく導入した擬似分子プローブの概念は、分子表面をプローブ分子で探索するという意味で、水分子プローブの拡張概念である。標的分子の表面を可能な限り精査し、そこからの影響を敏感に感じるためには、適切な化学構造を擬似分子プローブに採用しなければならない。すなわち、適切な擬似分子プローブを採用することで、我々は標的分子の表面を正確に探ることも可能である。本研究で種々の擬似分子プローブを試みた結果、シクロペンチルメチル基を複数の反応原子団に結合させたプローブが非常に有効に機能することが見出された。この擬似分子プローブの特徴は、反応原子団が効果的に標的分子の結合部位にある化学的および構造的な特徴を探査できることにある。本研究の結果は、擬似分子プローブの活用が標的分子に対する新規リガンドの発見に有用なだけでなく、様々な生体高分子の機能解析にも有効であることを強く示唆するものである。

5. 謝辞

第 36 回構造活性相関シンポジウムの発表において、貴重なご意見、ご指導を賜りました多くの先生方に心よりお礼申し上げます。本研究内容を本誌に掲載して頂く機会を与えてくださいました諸先生方に心よりお礼申し上げます。

6. 参考文献

(1) K.Toda, J.Goto and N.Hirayama *J. Chem. Inf. Model.*, to be submitted.
(2) H.M. Berman, J. Westbrook, Z. Feng, G. Gilliland, T.N. Bhat, H. Weissig, I.N. Shindyalov, P.E. Bourne *Nucleic Acids Research*, **2000**, *28*, 235-242.
(3) MOE (Molecular Operating Environment), Version 2007.0902; Chemical Computing Group Inc.: Montreal, Quebec, Canada **2007**.
(4) J. Goto, R. Kataoka, H. Muta and N. Hirayama *J. Chem. Inf. Model.*, **2008**, *48*, 583-590.
(5) K. Horio, H. Muta, J. Goto and N. Hirayama *Chem. Pharm. Bull.*, **2007**, *55*, 980-984.

Acta Crystallographica Section F
Structural Biology and Crystallization Communications
ISSN 1744-3091

Daisuke Nakayama, Youssef Ben Ammar and Soichi Takeda*

Department of Cardiac Physiology, National Cardiovascular Center Research Institute, Japan

Correspondence e-mail: stakeda@ri.ncvc.go.jp

Received 7 October 2009
Accepted 5 November 2009

Crystallization and preliminary X-ray crystallographic analysis of blood coagulation factor V-activating proteinase (RVV-V) from Russell's viper venom

Russell's viper venom blood coagulation factor V activator (RVV-V) is a thrombin-like serine proteinase that specifically activates factor V by cleaving a single peptide bond between Arg1545 and Ser1546. Activated factor V combines with activated factor X produced by the enzyme RVV-X in the venom to form the prothombinase complex, which can induce disseminated intravascular coagulopathy in envenomated animals. In the current study, RVV-V was crystallized in order to attempt to understand its substrate specificity for factor V. Four distinct crystal forms of RVV-V were obtained using the sitting-drop vapour-diffusion method and diffraction data sets were collected on SPring-8 beamlines. The best crystal of RVV-V generated data sets to 1.9 Å resolution.

1. Introduction

Blood coagulation factor V is a key component of the haemostatic system (Nicolaes & Dahlback, 2002). Factor V exists as a precursor molecule in the circulation and is converted to its active form, factor Va, after cleavage of the three peptide bonds between Arg709 and Ser710, between Arg1018 and Thr1019 and between Arg1545 and Ser1546 by thrombin or activated factor X (factor Xa; Mann & Kalafatis, 2003; Thorelli *et al.*, 1998). Factor Va acts as a nonenzymatic cofactor in the prothrombinase complex that converts prothrombin to thrombin. Factor Va also enhances the rate of prothrombin activation of factor Xa on phospholipid membranes. This rate is enhanced by about 300 000-fold and enhancement occurs in a Ca^{2+}-dependent manner (Nesheim *et al.*, 1979; Rosing *et al.*, 1980). Finally, thrombin converts soluble fibrinogen into insoluble fibrin, leading to blood-clot formation.

The venom of Russell's viper (*Daboia russelli siamensis*) has been recognized for its potent coagulation activity. Two major components of Russell's viper venom can collaboratively accelerate disseminated intravascular coagulation in the body of prey (Schiffman *et al.*, 1969). One of these components is RVV-X (EC 3.4.24.58), a heterotrimeric metalloproteinase that specifically activates factor X. We recently determined the crystal structure of RVV-X at 2.9 Å resolution and proposed a model for factor-X activation (Takeda *et al.*, 2007). The other component is RVV-V (EC 3.4.21.95), a thrombin-like serine proteinase that specifically activates factor V (Hjort, 1957). RVV-V cleaves the single peptide bond between Arg1545 and Ser1546, resulting in activation of factor V (Dahlback, 1986; Kane & Davie, 1986, 1988; Jenny *et al.*, 1987). RVV-V does not cleave the other two thrombin-susceptible sites of factor V. Furthermore, RVV-V is resistant to endogenous serine proteinase inhibitors (serpins) such as antithrombin, which regulates thrombin activity under physiological conditions (Segers *et al.*, 2006).

The molecular mechanism by which RVV-V recognizes and cleaves the Arg1545–Ser1546 bond of factor V is poorly understood, primarily owing to a lack of high-resolution structural information, although a homology model of RVV-V has previously been reported (Segers *et al.*, 2006). To gain insight into the molecular basis of its substrate recognition and serpin resistance, we crystallographically analyzed RVV-V. Here, we report the crystallization and preliminary crystallographic studies of RVV-V with and without inhibitors.

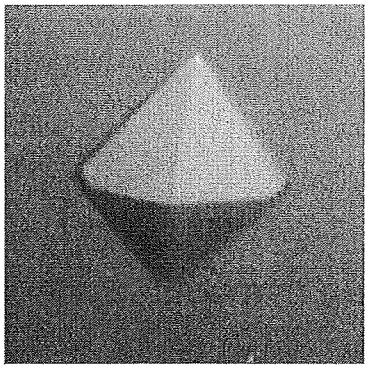

2. Materials and methods

2.1. Purification

D. russelli siamensis venom was purchased from the Japan Snake Institute. RVV-V was purified as described previously (Schiffman *et al.*, 1969; Kisiel, 1979) with some modifications. Lyophilized crude venom powder (200 mg) was dissolved in TBS buffer (10 m*M* Tris–HCl pH 7.5 and 150 m*M* NaCl) to a final concentration of 40 mg ml^{-1} and centrifuged at 15 000*g* for 30 min. The supernatant was loaded onto a HiPrep 26/60 Sephacryl S-100 HR column (GE Healthcare, UK) equilibrated with TBS buffer. Fractions containing RVV-V were pooled and applied onto a 1 ml Resource S column (GE Healthcare) pre-equilibrated with TBS buffer. Nonspecifically bound proteins were eluted with washing buffer (10 m*M* Tris–HCl pH 7.5 and 200 m*M* NaCl pH 7.5) and bound proteins were eluted with a linear gradient of NaCl (200–600 m*M*) in 10 m*M* Tris–HCl pH 7.5. The fractions containing RVV-V were pooled, dialyzed against 10 m*M* Tris–HCl, concentrated using Vivaspin (Sartorius, Germany) with a 10 000 nominal molecular-weight-limit membrane to give a protein concentration of 11.3 mg ml^{-1} and subjected to crystallization.

2.2. Crystallization

Preliminary screening of the crystallization conditions was performed with PEG/Ion 1, PEG/Ion 2, Crystal Screen 1 and Crystal Screen 2 kits (Hampton Research, USA) using the sitting-drop vapour-diffusion method at 277 and 293 K. Protein aliquots (0.1 µl at a concentration of 11.3 mg ml^{-1}) with or without the inhibitors Pefabloc [4-(2-aminoethyl)-benzenesulfonyl fluoride; 10 m*M*; Roche, Switzerland] or PPACK (D-Phe-Pro-Arg-chloromethylketone; 10 m*M*; Calbiochem, Germany) were mixed with 0.1 µl reservoir solution using a repeatable nanolitre pipetting device (Mosquito, TTP Labotech, UK). Droplets were equilibrated against 100 µl reservoir solution.

2.3. Crystallographic data collection

For X-ray measurements, crystals were cryoprotected, mounted in a nylon loop (Hampton Research, USA) or a Lytho Loop (Protein-Wave Corp., Japan) and immediately exposed to a stream of nitrogen gas at 100 K to flash-freeze the samples. The crystals were evaluated in-house using Cu $K\alpha$ radiation (λ = 1.5418 Å) generated by an RA-Micro 7 rotating-anode X-ray generator with an R-AXIS VII image-plate detector (Rigaku, Japan). High-resolution data sets were collected using a Rayonix MX225HE CCD detector installed on the BL41XU beamline at SPring-8. The images collected were processed using the *HKL*-2000 software (Otwinowski & Minor, 1997).

3. Results and discussion

3.1. Purification

RVV-V was purified from the crude venom of *D. russelli siamensis* using gel-filtration chromatography followed by cation-exchange chromatography. The homogeneity of the purified RVV-V was confirmed by SDS–PAGE in the presence or absence of 10 m*M* dithiothreitol (Laemmli, 1970). RVV-V consists of 236 amino acids with a molecular weight of 29 kDa (Tokunaga *et al.*, 1988). Consistent with this previous report, after two-step chromatography the purified RVV-V band was detected at about 29 kDa (Fig. 1). Approximately 4 mg RVV-V was purified from 200 mg crude venom.

3.2. Crystallization

RVV-V crystals were initially obtained under two distinct conditions. Form 1 crystals were obtained using solution No. 38 of the PEG/Ion 2 kit [50 m*M* citric acid, 50 m*M* bis-tris propane pH 5.0 and 20%(*w*/*v*) PEG 3350] at 293 K. Form 2 crystals were obtained using solution No. 47 of the PEG/Ion 2 kit [1%(*w*/*v*) tryptone, 0.05 *M* Na HEPES pH 7.0 and 12%(*w*/*v*) PEG 3350] at 293 K. Crystals of

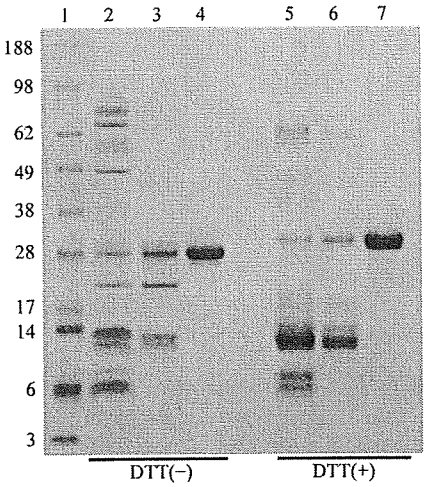

Figure 1
Purification of RVV-V. Crude venom (20 µg) and purified RVV-V (4 µg) were loaded on 4–12% SDS–PAGE in the presence or absence of 10 m*M* dithiothreitol. Proteins were stained with Coomassie Brilliant Blue. Lane 1, molecular-weight markers (kDa). Lanes 2 and 5, crude venom from *D. russelli siamensis*. Lanes 3 and 6, RVV-V purified by gel-filtration chromatography. Lanes 4 and 7, RVV-V purified by cation-exchange chromatography. Lanes 2–4 are under nonreducing conditions [DTT(−)] and lanes 5–7 are under reducing conditions [DTT(+)].

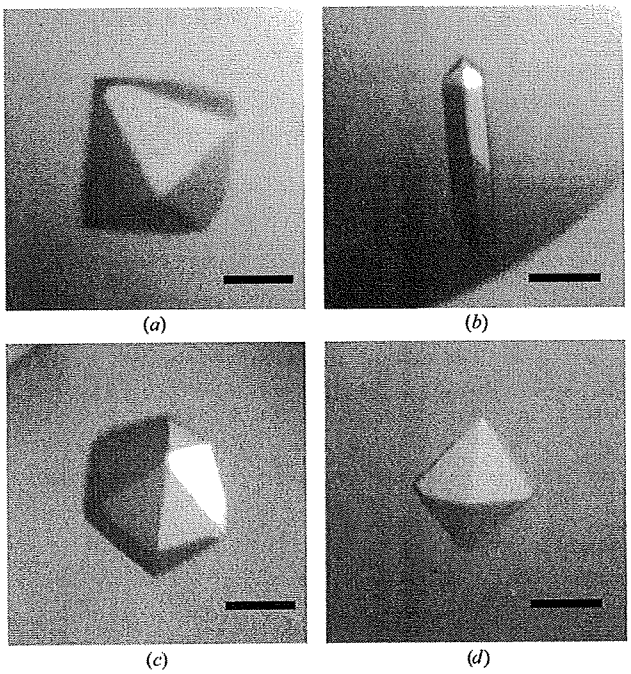

Figure 2
Crystals of RVV-V obtained under different conditions. (*a*) Form 1, (*b*) form 2, (*c*) form 3 (complexed with Pefabloc) and (*d*) form 4 (complexed with PPACK). The scale bar is 0.1 mm in length.

Table 1
Data-collection statistics for RVV-V crystals.

Values in parentheses are for the highest resolution shell.

	Form 1	Form 2	Form 3	Form 4
Inhibitor	None	None	Pefabloc	PPACK
X-ray source	SPring-8 BL41XU			
Space group	$P6_522$	$P6_522$	$P6_522$	$P6_522$
Unit-cell parameters				
a (Å)	78.9	80.1	78.9	77.2
b (Å)	78.9	80.1	78.9	77.2
c (Å)	157.3	160.4	160.6	168.4
$\alpha = \beta$ (°)	90	90	90	90
γ (°)	120	120	120	120
Resolution (Å)	50–1.9 (1.97–1.9)	50–1.9 (1.97–1.9)	30–2.85 (2.95–2.85)	30–2.55 (2.64–2.55)
No. of reflections	23547 (2301)	24182 (2389)	7400 (708)	10311 (993)
R_{merge}†	0.06 (0.255)	0.05 (0.282)	0.06 (0.319)	0.06 (0.267)
$I/\sigma(I)$	22.8 (8.64)	22.0 (7.13)	40.6 (12.3)	33.8 (15.8)
Completeness (%)	99.8 (100)	97.6 (99.5)	99.9 (100)	99.7 (100)
Redundancy	7	7.2	20.7	20.4
No. of molecules in ASU	1	1	1	1
Matthews value (Å^3 Da^{-1})	2.66	2.78	2.70	2.69
Solvent content (%)	53.9	55.8	54.6	54.2

† $R_{merge} = \sum_{hkl}\sum_i |I_i(hkl) - \langle I(hkl)\rangle| / \sum_{hkl}\sum_i I_i(hkl)$, where $I_i(hkl)$ is the ith intensity measurement of reflection hkl and $\langle I(hkl)\rangle$ is its average.

the RVV-V–Pefabloc and RVV-V–PPACK complexes were initially obtained in a similar manner as form 1 crystals using solution No. 38 of the PEG/Ion 2 kit at 293 K.

Because the crystals obtained from the initial screen were too small for X-ray analysis, we optimized the crystallization conditions to obtain larger single crystals by lowering the precipitant concentration and changing the droplet size and pH. Larger form 1 crystals were obtained by mixing 0.5 µl protein solution and 0.5 µl of a reservoir solution containing 50 m*M* citric acid, 50 m*M* bis-tris propane pH 5.0 and 16%(*w*/*v*) PEG 3350 (Fig. 2*a*). Larger form 2 crystals were obtained by mixing 0.3 µl protein solution and 0.3 µl of a reservoir solution containing 0.8%(*w*/*v*) tryptone, 0.04 *M* Na HEPES pH 7.0 and 9.6%(*w*/*v*) PEG 3350 (Fig. 2*b*). Diffraction-quality crystals of form 3 (RVV-V–Pefabloc complex) and form 4 (RVV-V–PPACK complex) were obtained by mixing 0.5 µl protein solution and 0.5 µl of a reservoir solution containing 0.8%(*w*/*v*) tryptone, 0.04 *M* Na HEPES pH 7.0 and 9.6%(*w*/*v*) PEG 3350 (Figs. 2*c* and 2*d*).

Crystals with dimensions of 200 × 200 × 200 µm (forms 1, 3 and 4) or 300 × 50 × 50 µm (form 2) were formed after 3–7 d at 293 K.

3.3. X-ray analysis

Prior to data collection, single crystals were cryoprotected using a reservoir solution supplemented with increasing glycerol concentrations (5, 10, 15 and 20%) in order to avoid osmotic shock-induced cracking. All diffraction data sets were acquired with a Rayonix MX225HE CCD detector using the oscillation method on beamline BL41XU, with an oscillation angle of 1.0°, a wavelength of 1.0 Å and a crystal-to-detector distance of 160 mm. The unit-cell parameters and statistics for the data sets are summarized in Table 1.

The asymmetric unit of each crystal was estimated to contain one RVV-V molecule, with corresponding crystal volume per protein weight ratios of 2.66, 2.78, 2.70 and 2.69 Å^3 Da^{-1} for crystal forms 1, 2, 3 and 4, respectively (Matthews, 1968). Solvent-content estimations based on a single copy of the molecule per asymmetric unit gave values of 53.9, 55.8, 54.6 and 54.2% for crystals forms 1, 2, 3 and 4, respectively. The unit-cell parameters of these four crystal forms were similar to, but distinct from, each other, suggesting structural changes that depended on the pH or on inhibitor binding. Clear molecular-replacement (MR) solutions for each crystal form were obtained in space group $P6_522$ using *MOLREP* from the *CCP*4 suite (Vagin & Teplyakov, 1997) with Ancrod (61% sequence identity), a snake-venom protein C activator from *Agkistrodon contortrix contortrix* (PDB code 2aiq; Murakami & Arni, 2005), as the structural model. Structural analyses of these crystals together with MR phasing are ongoing.

We thank Mariko Tomisako for her help in the purification and crystallization experiments and the staff of SPring-8 for assistance with data acquisition. This work was supported in part by grants-in-aid from the Ministry of Health, Labour and Welfare of Japan, grants-in-aid from the Ministry of Education, Culture, Sports, Science and Technology of Japan and by a grant from the Takeda Science Foundation.

References

Dahlback, B. (1986). *J. Biol. Chem.* **261**, 9495–9501.
Hjort, P. F. (1957). *Scand. J. Clin. Lab. Invest.* **9**, 1–183.
Jenny, R. J., Pittman, D. D., Toole, J. J., Kriz, R. W., Aldape, R. A., Hewick, R. M., Kaufman, R. J. & Mann, K. G. (1987). *Proc. Natl Acad. Sci. USA*, **84**, 4846–4850.
Kane, W. H. & Davie, E. W. (1986). *Proc. Natl Acad. Sci. USA*, **83**, 6800–6804.
Kane, W. H. & Davie, E. W. (1988). *Blood*, **71**, 539–555.
Kisiel, W. (1979). *J. Biol. Chem.* **254**, 12230–12234.
Laemmli, U. K. (1970). *Nature (London)*, **227**, 680–685.
Mann, K. G. & Kalafatis, M. (2003). *Blood*, **101**, 20–30.
Matthews, B. W. (1968). *J. Mol. Biol.* **33**, 491–497.
Murakami, M. T. & Arni, R. K. (2005). *J. Biol. Chem.* **280**, 39309–39315.
Nesheim, M. E., Taswell, J. B. & Mann, K. G. (1979). *J. Biol. Chem.* **254**, 10952–10962.
Nicolaes, G. A. & Dahlback, B. (2002). *Arterioscler. Thromb. Vasc. Biol.* **22**, 530–538.
Otwinowski, Z. & Minor, W. (1997). *Methods Enzymol.* **276**, 307–326.
Rosing, J., Tans, G., Govers-Riemslag, J. W., Zwaal, R. F. & Hemker, H. C. (1980). *J. Biol. Chem.* **255**, 274–283.
Schiffman, S., Theodor, I. & Rapaport, S. I. (1969). *Biochemistry*, **8**, 1397–1405.
Segers, K., Rosing, J. & Nicolaes, G. A. (2006). *Proteins*, **64**, 968–984.
Takeda, S., Igarashi, T. & Mori, H. (2007). *FEBS Lett.* **581**, 5859–5864.
Thorelli, E., Kaufman, R. J. & Dahlback, B. (1998). *Thromb. Haemost.* **80**, 92–98.
Tokunaga, F., Nagasawa, K., Tamura, S., Miyata, T., Iwanaga, S. & Kisiel, W. (1988). *J. Biol. Chem.* **263**, 17471–17481.
Vagin, A. & Teplyakov, A. (1997). *J. Appl. Cryst.* **30**, 1022–1025.

Crystal structures of the noncatalytic domains of ADAMTS13 reveal multiple discontinuous exosites for von Willebrand factor

Masashi Akiyama[a,1], Soichi Takeda[a,1,2], Koichi Kokame[a], Junichi Takagi[b], and Toshiyuki Miyata[a,2]

[a]National Cardiovascular Center Research Institute, Suita, Osaka 565-8565, Japan; and [b]Laboratory of Protein Synthesis and Expression, Institute for Protein Research, Osaka University, Suita, Osaka 565-0871, Japan

Edited by Philip W. Majerus, Washington University Medical School, St. Louis, MO, and approved September 16, 2009 (received for review August 27, 2009)

ADAMTS13 specifically cleaves plasma von Willebrand factor (VWF) and thereby controls VWF-mediated platelet thrombus formation. Severe deficiencies in ADAMTS13 can cause life-threatening thrombotic thrombocytopenic purpura. Here, we determined 2 crystal structures of ADAMTS13-DTCS (residues 287–685), an exosite-containing human ADAMTS13 fragment, at 2.6-Å and 2.8-Å resolution. The structures revealed folding similarities between the disintegrin-like (D) domain and the N-terminal portion of the cysteine-rich domain (designated the C_A domain). The spacer (S) domain forms a globular functional unit with a 10-stranded β-sandwich fold that has multiple interaction sites with the C_A domain. We expressed 25 structure-based mutants of ADAMTS13-MDTCS (residues 75–685) and measured their enzymatic activity. We identified 3 VWF-binding exosites on the linearly aligned discontinuous surfaces of the D, C_A, and S domains traversing the W-shaped molecule. Since the MDTCS domains are conserved among ADAMTS family proteins, the structural framework of the multiple enzyme-substrate interactions identified in the ADAMTS13-VWF system provides the basis for a common substrate recognition mode in this class of proteinases.

hemostasis | metalloproteinase | modular protein | substrate recognition

The human ADAMTS (*a d*isintegrin-like *a*nd *m*etalloproteinase with *t*hrombo*s*pondin type-1 motif) family is composed of 19 genes that encode extracellular multidomain enzymes containing a reprolysin-type metalloproteinase domain and several conserved domains following the metalloproteinase domain (1). In contrast to the phylogenetically related ADAM (*a d*isintegrin *a*nd *m*etalloproteinase) family proteins, most of which have a transmembrane and a cytoplasmic domain in the C-terminal region (2), ADAMTSs are secretary proteinases that lack these domains and instead have at least 1 thrombospondin-1 (TSP-1) type-1 repeat (TSR). ADAMTSs have diverse functions including procollagen processing, aggrecan degradation, and organogenesis (1). ADAMTS13 controls platelet thrombus formation through cleavage of the von Willebrand factor (VWF).

VWF is a plasma glycoprotein that plays an essential role in platelet-dependent hemostasis (3, 4). VWF mediates platelet adherence to damaged blood vessels through interactions with glycoprotein Ib on the platelet surface and collagen in the subendothelium and contributes to platelet aggregation through interactions with integrin $\alpha_{IIb}\beta_3$. VWF, synthesized mainly in vascular endothelial cells, contains 2,050 aa residues and is released into the plasma as disulfide-bonded ultralarge VWF (UL-VWF) multimers having a mass greater than 20,000 kDa. In healthy individuals, UL-VWF multimers undergo limited proteolytic processing (5). ADAMTS13 specifically cleaves the Tyr-1605-Met-1606 peptidyl bond within the A2 domain of VWF (6) in a fluid shear-stress-dependent manner (7). Because VWF multimers have an alternate head-to-head and tail-to-tail disulfide-bonded architecture between neighboring subunits, cleavage by ADAMTS13 gives rise to a series of circulating multimers with molecular masses ranging from 500 to 15,000 kDa. Control of the size distribution of VWF multimers is important for normal hemostasis, as large multimers are hemostatically more active than small multimers (3). Deficiencies in ADAMTS13 activity, caused either by genetic mutations in the ADAMTS13 gene or by acquired inhibitory autoantibodies directed against the ADAMTS13 protein, results in the accumulation of UL-VWF in the plasma (8–11). The UL-VWF accumulation leads to the formation of disseminated platelet-rich microthrombi in the microvasculature, which results in the life-threatening disease, thrombotic thrombocytopenic purpura (TTP).

The human ADAMTS13 gene encodes a precursor protein of 1,427 aa with a modular structure consisting of a signal peptide, a propeptide (P), a metalloproteinase (M) domain, a disintegrin-like (D) domain, a TSR (T1), a cysteine-rich (C) region, a spacer (S), 7 TSRs (T2–T8), and 2 CUB (*c*omplement components C1rC1s/*u*rinary epidermal growth factor/*b*one morphogenetic protein-1) domains (11–13). The M domain of ADAMTS13 alone is not sufficient for recognition and specific cleavage of VWF, but full VWF-cleaving activity is achieved in vitro with an M-D-T1-C-S domain fragment (14–17). In addition, antibodies isolated from idiopathic TTP patients commonly inhibit ADAMTS13 activity by binding to the C and S domains of ADAMTS13 (14, 18, 19). Collectively, these observations indicate that the noncatalytic domains, especially the proximal C-terminal domains including the D, T1, C, and S domains (designated ADAMTS13-DTCS), are essential for recognition of VWF. The crystal structures of the MD domains (ADAMTS-MDs) of ADAMTS1 (20), ADAMTS4 (21), and ADAMTS5 (21) have been determined, but no structural information is currently available for the T1, C, and S domains of ADAMTS proteins. To gain insight into the molecular mechanism of VWF recognition by ADAMTS13, we solved the crystal structures of ADAMTS13-DTCS (residues 287–685) and performed a series of structure-based mutagenesis experiments to identify VWF-binding exosites. The present structure is the first for the TCS domains of any ADAMTS family member and will provide a template for understanding the role of these domains in substrate recognition by ADAMTS proteins.

Results

Structure Determination. The structure of ADAMTS13-DTCS was solved using the multiple-wavelength anomalous dispersion

Author contributions: M.A., S.T., K.K., J.T., and T.M. designed research; M.A. and S.T. performed research; M.A., S.T., and K.K. analyzed data; and M.A., S.T., and T.M. wrote the paper.

The authors declare no conflict of interest.

This article is a PNAS Direct Submission.

Data deposition: The atomic coordinates and structure factors have been deposited in Protein Data Bank, www.pdb.org [PDB ID codes 3GHM (form-1 ADAMTS13-DTCS) and 3GHN (form-2 ADAMTS13-DTCS)].

[1]M.A. and S.T. contributed equally to this work.

[2]To whom correspondence may be addressed. E-mail: stakeda@ri.ncvc.go.jp or miyata@ri.ncvc.go.jp.

This article contains supporting information online at www.pnas.org/cgi/content/full/0909755106/DCSupplemental.

www.pnas.org/cgi/doi/10.1073/pnas.0909755106

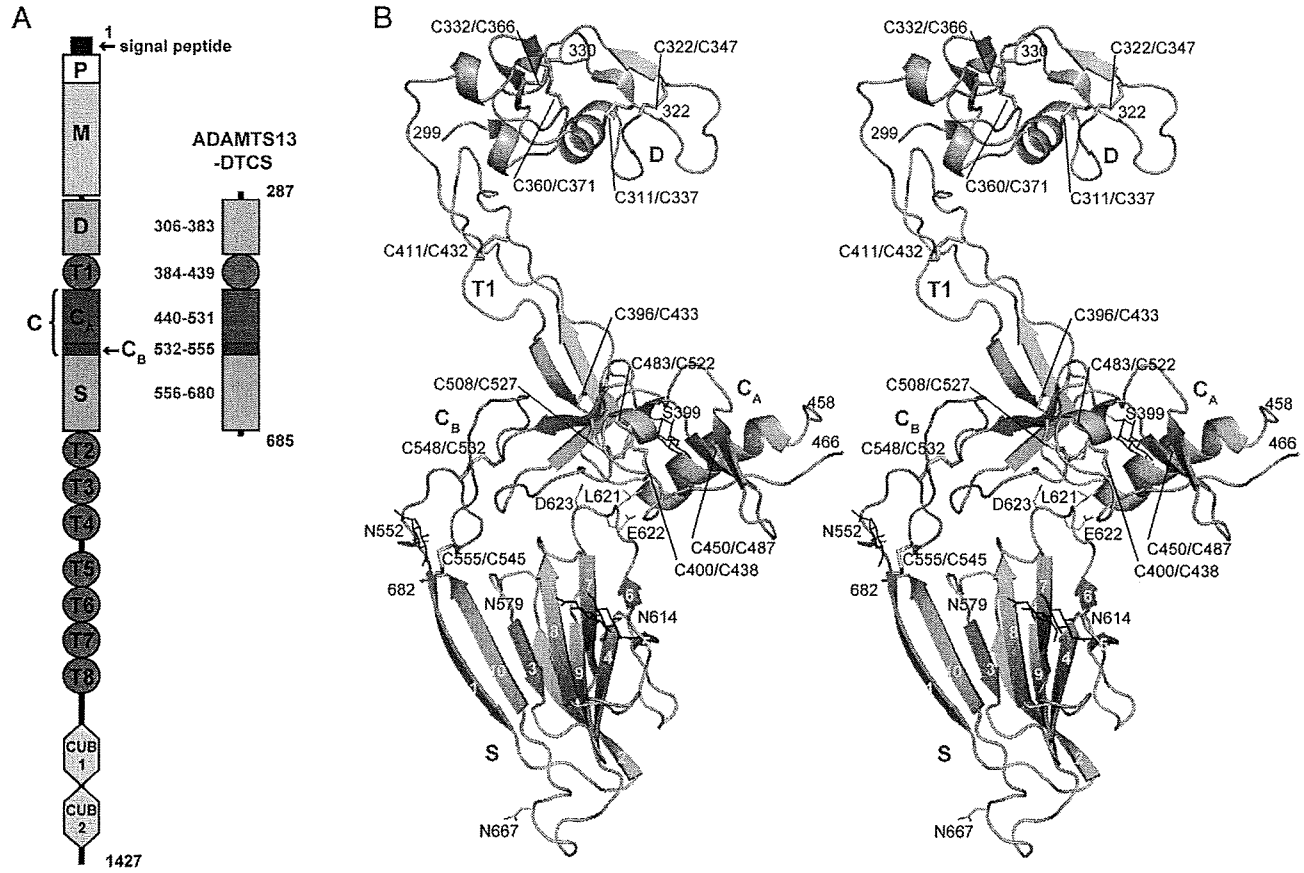

Fig. 1. Structure of ADAMTS13-DTCS. (*A*) Schematic representation of the domain structures of full-length ADAMTS13 and ADAMTS13-DTCS. (*B*) Ribbon structure of ADAMTS13-DTCS (form-1) in stereo. Domains are colored as in *A*. Strands in the S domain are numbered.

(MAD) method at 2.9 Å using data sets obtained from a single osmium derivative crystal (Table S1). The structure was further refined against 2 native data sets, form-1 (space group $C2$, a = 152.7 Å, b = 52. 9 Å, c = 76.2 Å, and β = 111.4°) and form-2 (space group $C2$, a = 138.6 Å, b = 51.4 Å, c = 76.4 Å, and β = 106.7°) at 2.6-Å (R = 0.243; R_{free} = 0.289) and 2.8-Å (R = 0.229; R_{free} = 0.280) resolution, respectively (Table S1). Each crystal contained 1 ADAMTS13-DTCS molecule per asymmetric unit. The final model of the form-1 (form-2) crystal includes ADAMTS13 residues 299–322 (323), 331 (330)-458, and 466–682. Electron densities for carbohydrate moieties attached to 3 of the 4 potential *N*-linked (Asn-552, Asn-579, and Asn-614) and one *O*-linked (Ser-399) site were observed (*SI Text* and Fig. S1). Pro-379, Pro-414, Pro-475, and Pro-618, were in the *cis* conformation.

Overall Structure. The N-terminal portion of the C domain (residues 440–531, designated the C_A domain here) in ADAMTS13 has a fold structurally homologous to that of the C domain of ADAMs, despite the lack of sequence similarity. The D domain (residues 306–383) of ADAMTS13 also has a fold similar to the C domain of ADAMs, which is consistent with recent crystallographic studies (20–22). Therefore, ADAMTS13 possesses 2 homologous domains that belong to the ADAM_CR family (Pfam database entry: pfam08516). The remaining C-terminal portion of the C domain (residues 532–555) is highly conserved in amino acid sequence among ADAMTS family proteins (Fig. S2, here called the C_B domain). The domain architecture of ADAMTS13 is schematically represented in Fig. 1*A*.

The overall structure of ADAMTS13-DTCS resembles a distorted W-shape, in which 3 knobs, the D, C_A, and S domains, are connected by 2 elongated structural modules, T1 and C_B (Fig. 1*B*). The homologous D and C_A domains are separated and related by a pseudo-90° screw rotation with an ≈45-Å translation along T1 (Fig. 1*B*). T1 has a very similar structure to that of the prototypical TSR, TSR2, in TSP-1 (23) with an rmsd of 1.37 Å for the equivalent Cα atoms (Fig. S1) and an antiparallel 3-stranded fold. Although the C_B domain has no apparent secondary structure, it has a series of turns stabilized by a pair of disulfide bonds (Cys-532-Cys-548 and Cys-545-Cys-555) and forms a rod shape with its N and C termini ≈25 Å apart (Fig. 1*B*). The C_A and S domains, bridged by the C_B domain, make direct contact through the extended loop of the S domain (Fig. 1*B* and *SI Text*). The structures of ADAMTS13 obtained from the 2 crystal forms are essentially the same, with the exception of the relative orientations between the domains (*SI Text* and Fig. S3). The structural details of the D, C_A, and S domains are described in the following sections and T1 in *SI Text*.

Comparison of the D and C_A Domains. The D and C_A domains have only 17% identity in their amino acid sequences (Fig. S2); however, their tertiary structures are quite similar (Fig. 2 *A*, *B*, and *E*). They share an N-terminal α-helix, 2 pairs of double-stranded antiparallel β-sheets, and 3 disulfide bonds, constituting the core structure of these domains. The D domain has an additional disulfide bond (Cys-322-Cys-347) that is strictly conserved among the ADAM counterparts (22, 24). The 3 peripheral loops differ markedly in structure between D and C_A in

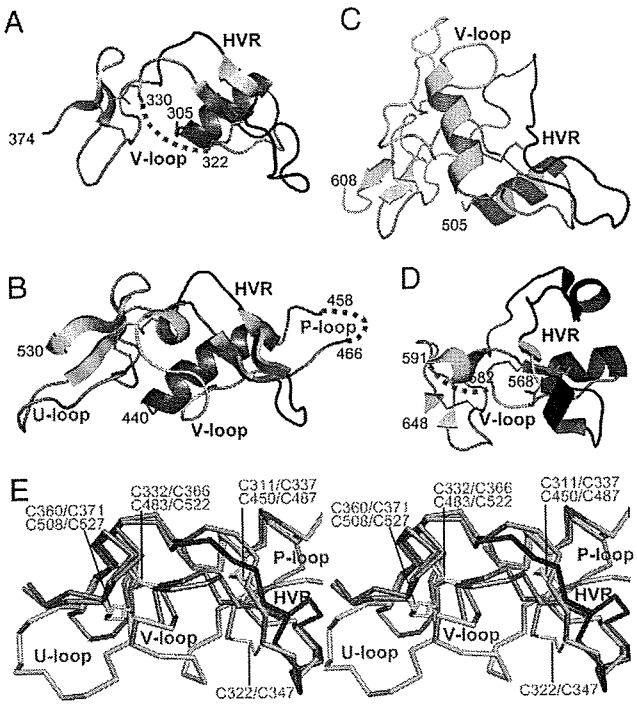

Fig. 2. Comparison of the D and C_A domain structures. Ribbon representation of the D (*A*) and C_A (*B*) domains of ADAMTS13-DTCS, and the C domains of VAP1 (representative of canonical ADAMs, PDB 2ERO) (*C*) and ADAM10 (PDB 2AO7) (*D*). The conserved α-helix, β-strands, and disulfide bonds are shown in red, yellow, and orange, respectively. The V-loop and HVR are shown in gray and blue, respectively. Disordered regions in the crystals are shown as dotted lines. The numbers of the terminal amino acid residues are indicated. (*E*) Superimposition of the D (orange) and C_A (green) domains in stereo. Disulfide bonds are indicated in stick representations.

ADAMTS13 (Fig. 2*E*). The amino acid sequences of these loops are also quite different between D and C_A in ADAMTS13 and in other ADAMTS family members (Fig. S2).

The loop following the first α-helix of the C_A domain (residues 454–469) is 12 aa residues longer than that of the D domain, protrudes from the main body of C_A, and is disordered along the distal side (Fig. 2 *B* and *E*). We designated this C_A-specific loop as the protruding (P) loop. One region in the D domain (residues 323–329) is disordered (Fig. 2*A*), not only in the current ADAMTS13 structures, but also in other reported ADAMTS1 structures (20), although the corresponding region of C_A is clearly defined in electron density maps. We designated this loop the variable (V) loop because of its variability in both length and amino acid sequence (Fig. S2). Canonical ADAM family members have a helix-loop insertion of 26–30 aa residues in the V-loop (Fig. 2*C*), whereas the atypical ADAM10 does not, and its C domain is more similar to the D and C_A domains of ADAMTS13, except for the hypervariable region (HVR) (Fig. 2*D*) (22, 24). ADAMTS13 has an insertion of 6 residues (residues 512–517) just before the C-terminal β-sheet of C_A (Fig. 2 *B* and *E*), which is not found in other ADAMTS members (Fig. S2). We designated this loop the ADAMTS13-C_A-unique (U) loop. Each C domain contains a HVR that differs markedly among ADAMs and may play a central role in substrate recognition (22, 24). ADAMTS13 has shorter HVRs in both the D and the C_A domains than those present in the ADAMs (Fig. 2 *A–D*). These loops and HVRs were targeted for mutations (see below).

There is an Arg-498-Gly-499-Asp-500 integrin recognition sequence in the C_A domain. The side chain of Arg-498 is buried and unavailable for protein–protein interactions, but the Asp-500 side chain is exposed toward the solvent.

Spacer Domain. The S domain is a long cysteineless segment and its primary structure shows no apparent homology to known structural motifs. The present study revealed that this region folds into a single globular domain with 10 β-strands in a jelly-roll topology, forming 2 antiparallel β-sheets that lie almost parallel to each other (Fig. 1*B* and Fig. S4*A*). The hydrophobic residues forming the core of the β-sandwich (Fig. S4*B*), a cluster of aromatic residues located on the concave outer surface of the smaller 4-stranded sheet (Fig. S4*C*), and proline and glycine residues in the loops, are highly conserved among ADAMTS proteins (Fig. S4*D*). Collectively, these findings suggest that ADAMTS proteins share the S domain architecture observed in ADAMTS13. In contrast, loops located at the distal side of the molecule are highly variable in both length and amino acid sequence among ADAMTS family members (Fig. S4*D*). The N and C termini of the S domain are in close proximity and thus the T2 following the S domain should be in close proximity to the C_A/S-domain junction but not the distal side of the S domain.

MDTCS Model. The reported crystal structures of the ADAMTS-MDs and our current ADAMTS13-DTCS structure enabled us to build an ADAMTS13-MDTCS model (Fig. 3*A*). The currently available ADAMTS-MD structures (20, 21) superimpose well on each other, except for subtle differences in the relative orientations of the M and D domains. We performed a functional assay using the ADAMTS13-MDTCS mutants F216E and A258C/K368C, which have modified interactions between the M and D domains. The results suggest that a stable association between the M and D domains is necessary for ADAMTS13 function (Fig. 3 *B* and *D* and *SI Text*).

VWF-Binding Exosites. We introduced mutations into ADAMTS13-MDTCS and measured the enzymatic activities of the mutants using the synthetic fluorogenic substrate FRETS-VWF73 (25). The results are summarized in Fig. 3 *C* and *D*.

In the current model, the D domain abuts the M domain catalytic site (Fig. 3*B*), suggesting that the surface of the D domain leading to the catalytic site functions as a VWF-binding exosite. Two mutants, 1 with a substitution in the HVR (D), R349D, and the other with 7 residues in the V-loop (D) replaced by a 4-residue linker, the ΔV-loop (D), exhibited diminished enzymatic activity (Fig. 3 *C* and *D*). The disordered V-loop (D) contains 4 charged residues, Arg-326, Glu-327, His-328, and Asp-330, which are suggested to lie in the vicinity of Arg-349 in the HVR (Fig. 3*B*). The cluster of these charged residues may collaboratively create an exosite (exosite-1). Charged amino acid-to-alanine substitutions revealed that Asp-1614, Glu-1615, and Lys-1617 in the VWF A2 domain act synergistically in ADAMTS13-mediated cleavage (26), suggesting that these charged residues in VWF are targets for exosite-1. Recently, Arg-349 was suggested to interact directly with VWF, most probably with Asp-1614 (27). Leu-350 and Val-352, which form a cluster of hydrophobic residues adjacent to the end of the catalytic cleft (Fig. 3*B*), also interact with VWF (27). This observation suggests that the hydrophobic cluster functions as a part of exosite-1.

The C_A domain has 3 surface loops. The ΔV-loop (C_A) mutant resulted in very low enzymatic activity (Fig. 3 *C* and *D*), suggesting that the V-loop (C_A) creates another exosite (exosite-2). A triple alanine substitution in the V-loop (C_A), H476A/S477A/Q478A, and a mutant at the N terminus of the HVR (C_A) adjacent to the V-loop (C_A), R488E, had significantly reduced activity (≈21%), suggesting that these hydrophilic or charged residues play a pivotal role in VWF recognition at exosite-2. The ΔU-loop and the F494Q/M496Q mutants showed reduced activity (≈40%) compared to the ΔP-loop mutant (≈53%). The

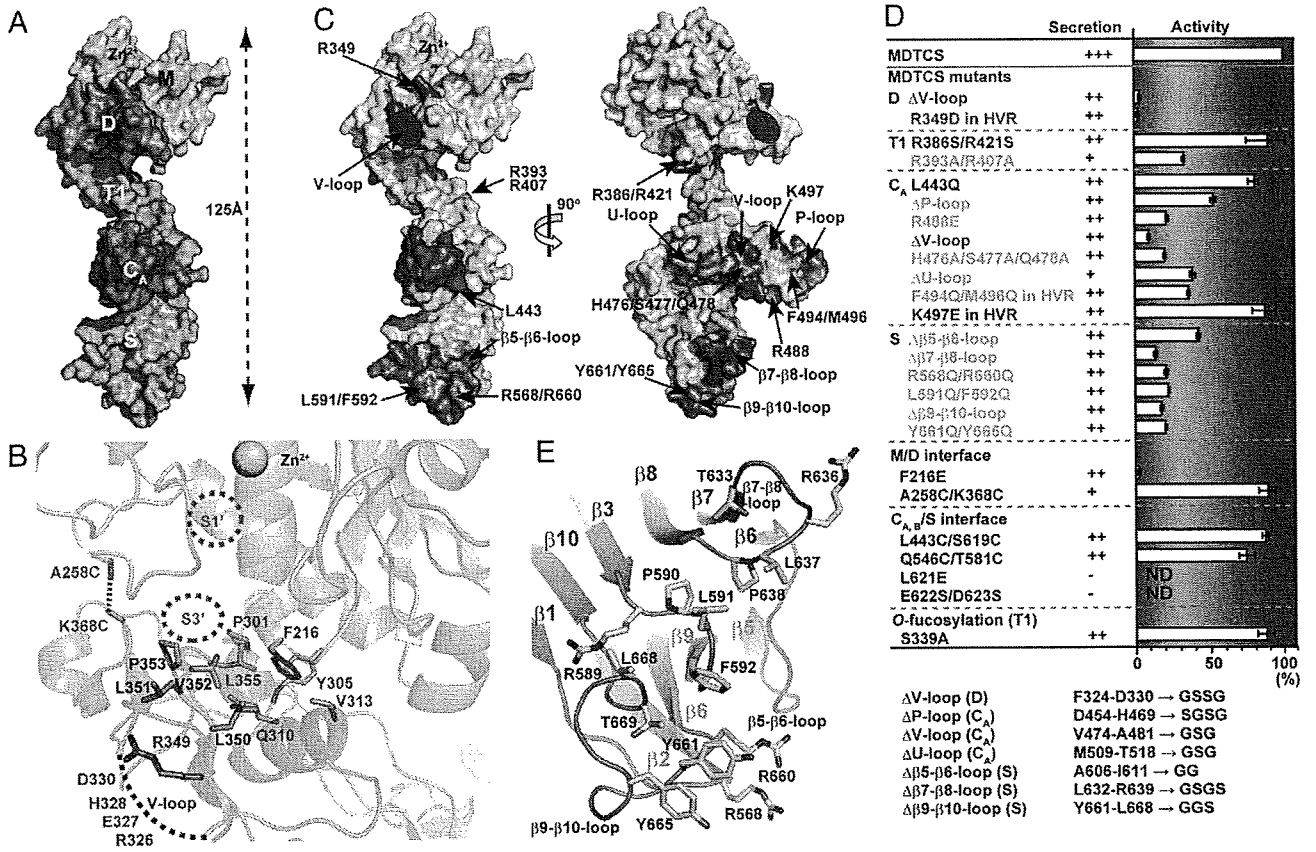

Fig. 3. A model of ADAMTS13-MDTCS and the residues affecting enzymatic activity. (*A*) Surface representation of the ADAMTS-MDTCS model. The M domain is shown in gray and the other domains are colored as in Fig. 1. The zinc ion is shown in yellow. (*B*) Close-up view of the interface between the M and D domains in the ADAMTS13-MDTCS model. Potential S1′ and S3′ substrate-binding sites, disordered V-loop (represented by a red dotted line), and the residues substituted by cysteine to form an interdomain disulfide bond (represented by a green dotted line) are indicated schematically. (*C*) The residues that affect ADAMTS13-MDTCS activity are indicated on the molecular surface, using a red-through-blue color-coding according to the results of the mutational assay shown in *D*. The molecule is viewed from 2 orthogonal directions. The V-loop of the D domain was disordered in the structures determined in this study and is represented by a red ellipsoid. (*D*) Summary of the mutational analysis, presenting the effects on secretion and enzymatic activity of the ADAMTS13-MDTCS mutants. Signs denote relative secretion level as follows: −, no detectable secretion; +, less than 30%; ++, 30≈70%; +++, 70~100% of the secretion level of the wild type; ND, not determined. Relative enzymatic activities of the mutants are shown in the bar graph. The error bars indicate the range. (*E*) Close-up view of the hydrophobic cluster surrounded by arginine residues (exosite-3) in the S domain.

U-loop (C_A) and residues 494–496 flank the V-loop (C_A) and may contribute to exosite-2. In contrast, the P-loop is distant from the V-loop (C_A) and may contribute less to VWF binding. A mutation in the middle of the HVR (C_A), K497E, maintained enzymatic activity comparable to wild type, even though Lys-497 is the equivalent of Arg-349, the pivotal residue in exosite-1 in the homologous D domain.

The 3 distal loops in the S domain were replaced by short linkers and enzymatic activity in the mutants was assayed. The Δβ7-β8-loop and Δβ9-β10-loop mutants showed greatly reduced activity compared to the Δβ5-β6-loop mutant (Fig. 3 *C* and *D*). The β9-β10 loop contains 2 tyrosine residues, Tyr-661 and Tyr-665, which face the solvent. The Y661Q/Y665Q mutant was significantly less active (≈18%) than the wild type. These tyrosine residues and Leu-668 in the β9-β10 loop form a hydrophobic cluster together with residues in the neighboring β3-β4 and β7-β8 loops (Pro-590, Leu-591, Phe-592, Leu-637, and Pro-638) (Fig. 3*E*). Leu-591 and Phe-592 are located at the center of this hydrophobic cluster. The L591Q/F592Q mutant showed reduced activity (Fig. 3*D*). Four arginine residues surround the hydrophobic cluster (Fig. 3*E*). The R568Q/R660Q mutant was significantly less active than the wild type. Collectively, the hydrophobic cluster rimmed with arginine residues in the S domain may to be another VWF-binding exosite (exosite-3).

Mutations of residues (R386S/R421S and L443Q) located apart from the exosites and the *O*-linked fucosylation site (S339A) did not affect activity. The R393A/R407A mutation in T1 showed reduced activity (≈33%). Arg-407 is located at the bottom of a cleft formed between exosite-1 and exosite-2. This residue may also contribute to VWF binding.

Discussion

This study presents a structural determination of the ADAMTS13 DTCS domains, which constitute important functional part of the proteinase. The structure revealed that the residues important for stabilizing the DTCS core architecture are strictly conserved in all ADAMTS proteins. In contrast, peripheral loops within the D, C_A, and S domains were substantially different in both length and amino acid sequence among ADAMTSs, suggesting that these regions have specific functions that distinguish each ADAMTS member. By systematic mutagenesis, we identified 3 VWF-binding exosites in these loops (Fig. 3*C*). The exosites are highly conserved among ADAMTS13s from different species (Fig. S5). The 3 exosites were linearly aligned in the 3D structure, traversing the W-shaped ADAMTS13-DTCS molecule (Fig. 3*C*). This arrange-

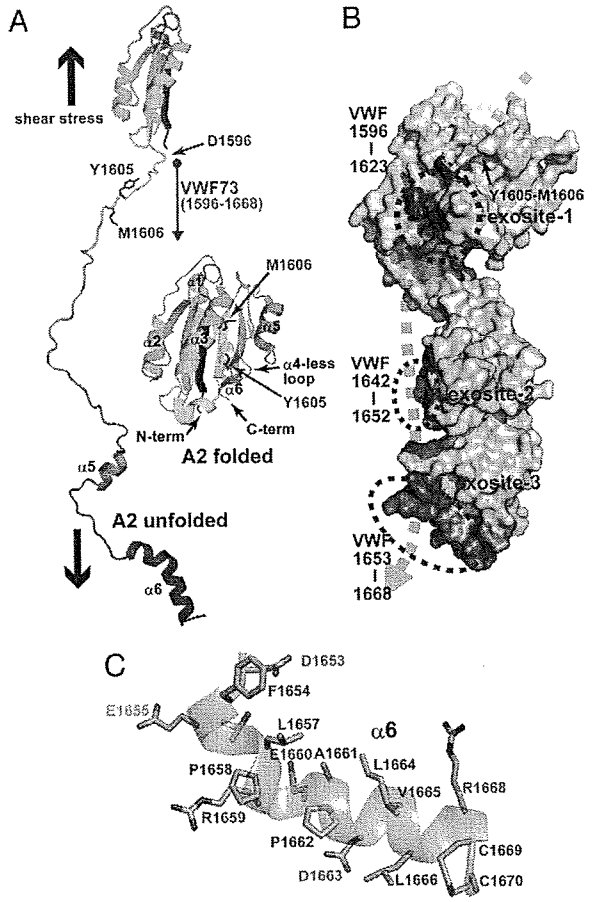

Fig. 4. ADAMTS13-VWF interactions. (*A*) Folded and unfolded structures of the VWF A2 domain. The VWF A2 domain adopts a Rossman fold with a central 6-stranded β-sheet surrounded by 5 α-helices (shown as "A2 folded") (28). The scissile peptide bond (Tyr-1605-Met-1606) is buried within the protein core under static conditions. The C-terminal region (residues 1,596–1,668, corresponding to VWF73) (31) of the A2 domain must be unfolded to expose the scissile bond and the exosite-binding regions under shear-stress conditions (shown as A2 unfolded). (*B*) ADAMTS13-MDTCS-VWF binding model. The molecular surface of the ADAMTS13-MDTCS model is shown in gray and the bound zinc ion is shown in yellow. Residues that mediate VWF binding are depicted as in Fig. 3*C*, and the exosites and the catalytic cleft are indicated by red and yellow dotted ellipsoids, respectively. The dotted green line represents a VWF molecule (residues 1,596–1,668) bound to ADAMTS-MDTCS. (*C*) Close-up view of the α6 helix and surrounding residues in the VWF A2 domain. Hydrophobic residues are indicated with red letters. Systematic charge-to-alanine substitutions revealed that the D1653A and D1663A mutations (cyan) reduced the substrate cleavage, the E1655A mutation (orange) slightly increased cleavage, and the R1659A, E1660A, and R1668A mutations (gray) had no significant effect (34).

ment suggests that these exosites bind collaboratively to multiple discontinuous regions of VWF.

A recent crystallographic study revealed that the Tyr-1605-Met-1606 scissile bond of VWF is buried within the core of the globular A2 domain under static conditions (Fig. 4*A*, A2 folded) (28). When VWF is subjected to fluid shear stress in circulation or denaturants in vitro, the A2 domain unfolds and adopts a partially extended conformation that makes its scissile peptide bond accessible for cleavage by ADAMTS13 (7, 29, 30) (Fig. 4*A*). We previously identified VWF73 (residues 1,596–1,668) as a minimum specific substrate for ADAMTS13 and suggested that a segment (residues 1,660–1,668) of VWF73 contains essential residues for recognition by ADAMTS13 (31). VWF73 is more than 200 Å long at its maximum extension, which is almost twice the distance between the catalytic site and the distal exosite-3 in the current ADAMTS13-MDTCS model. NMR spectroscopy has indicated that VWF73 adopts an unfolded structure (5). Therefore, the ADAMTS-MDTCS appears to be able to accommodate, by an induced-fit mechanism, a partially unfolded VWF73 segment along the extended molecular surface encompassing at least 3 critical exosites (Fig. 4*B*). Exosite-3 forms a cluster of hydrophobic residues rimmed by basic residues (Fig. 3*E*). Both the surface properties and the size of exosite-3 imply that exosite-3 binds to VWF, such that the VWF segment (residues 1,653–1,668) forms an amphipathic α-helix (α6 as in the crystal structure, Fig. 4*C*) and makes contact with ADAMTS13 by facing its hydrophobic residues toward exosite-3. Autoantibodies that inactivate ADAMTS13 are the most frequent cause of acquired TTP. These TTP patients possess antibodies directed against ADAMTS13 residues 657–666 (32) that exactly coincide with the β9-β10 loop, a part of exosite-3.

The present structure suggests a linear correspondence between the ADAMTS13 domains and their interaction sites in the A2 domain of VWF, consistent with previous systematic mutagenesis studies and kinetic analysis by Gao et al. (33). These authors suggested that the S domain contains an exosite that primarily determines catalytic efficiency by interacting with α6 of the VWF A2 domain (33). They identified 3 other VWF segments that interact with the MD, T1, and C domains of ADAMTS13 (17). Our structural and functional data are in good agreement with these observations, suggesting that the catalytic cleft plus exosite-1, exosite-2, and exosite-3 make cooperative, modular contacts with 3 discrete segments of the VWF A2 domain, the residues flanking the cleavage site (P9-P18′, residues 1,596–1,623), residues 1,642–1,652 and the α6 (residues 1,653–1,668) of the A2 domain, respectively (Fig. 4*B*). The model is also consistent with the previous observation that decreasing the length of peptides derived from the C terminus of the VWF A2 domain caused a progressive decrease in their potency as ADAMTS13 inhibitors (34). The elongated structure of the stiff, rod-like T1 module and its nonessential interactions with VWF (17) suggest that its primary role is to position the exosites spatially. The mobility of the domains (Fig. S3 and *SI Text*) suggests that a spectrum of ADAMTS13 conformations exist, with different spatial alignments of the exosites, increasing the possibility of ADAMTS13 interacting with partially unfolded VWF molecules, which also present a wide spectrum of conformations under shear-stress conditions in the circulation. The M domains of ADAMTS4 and ADAMTS5 do not retain specific catalytic activity. The inclusion of the proximal C-terminal domains enhances their aggrecanase activity, suggesting that these ADAMTSs function through multiple exosites (35–39), as observed in the ADAMTS13-VWF system.

More than 80 causative mutations for congenital TTP have been identified in the ADAMTS13 gene (11, 40, 41), including 16 missense mutations within the DTCS region. These mutations are not restricted to a specific region but are located throughout the molecule, suggesting that most of the mutations cause some structural defect that affects proper folding and secretion (Table S2). The R349C and P353L mutants, however, are likely to affect enzymatic activity: Arg-349 is in exosite-1 and Pro-353 forms part of the potential substrate-binding S3′ pocket (Fig. 3*B*). Five polymorphisms have been identified within the DTCS region (Table S2). Approximately 10% of the Japanese population are heterozygous for P475S substitution, located in the V-loop (C_A), which reduces VWF-cleaving activity (40, 42). The P618A substitution reduces secretion efficiency in cultured cells (43). Both proline residues adopt the *cis* conformation and, therefore, substitution by nonproline residues would cause structural distortions.

Shear stress in the blood circulation controls the exposure of the cryptic scissile bond and exosite-binding regions in VWF to ADAMTS13. The M domain of ADAMTS13 is catalytically

active, whereas the noncatalytic domains display surface features that are optimized for recognizing an unfolded VWF A2 domain. Therefore, cleavage by ADAMTS13 is primarily dependent on shear-force-induced unfolding of the VWF molecule. The force-induced proteolysis observed for ADAMTS13-VWF represents a model for probing the molecular mechanisms underlying the translation of a mechanical stimulus into a chemical response in a biological system.

Materials and Methods

Preparation, Crystallization and Structural Analysis of ADAMTS13-DTCS. Production and crystallization of ADAMTS-DTCS has been described previously (44). Briefly, ADAMTS13-DTCS (residues 287–685), with a C-terminal tobacco etch virus proteinase cleavage site followed by tandem His-tag sequences, was expressed in CHO Lec 3.2.8.1 cells. After purification on a Ni-NTA column, ADAMTS13-DTCS was subjected to proteolysis with the tobacco etch virus proteinase and was further purified using HiTrap SP (GE Healthcare). ADAMTS13-DTCS crystals were obtained by the sitting drop vapor diffusion method, with drops containing 0.5 μL protein solution and 0.5 μL reservoir solution (26% (wt/vol) PEG1500, 100 mM Mes, pH 6.0) supplemented with 0.2 μL of 40% (wt/wt) pentaerythritol ethoxylate (3/4 EO/OH) (Hampton Research) equilibrated for several days at 293 K. Os-derivative crystals were obtained by soaking native crystals in reservoir solution supplemented with 1 mM $OsCl_3$ and 20% glycerol for several hours. Crystals were cryoprotected in reservoir solution supplemented with 20% glycerol and flash cooled under a stream of nitrogen gas at 100 K. All diffraction data were collected at the SPring-8 beamline BL41XU (Table S1). Details of structural analysis are described in *SI Text*.

Functional Analysis. Recombinant wild-type and 25 mutants of ADAMTS13-MDTCS (residues 75–685) with a C-terminal His-tag were prepared by transient expression using a cytomegalovirus promoter-driven expression vector and HeLa cells. The culture medium and cell lysates were collected 72 h posttransfection, and the expression levels were quantified by Western blotting using anti-His-tag (Fig. S6). For enzyme assays, culture medium (5 μL) containing equivalent amounts of ADAMTS13-MDTCSs was mixed with reaction mixture (95 μL) containing 2 μM fluorogenic substrate (FRETS-VWF73) (25), 10 mM Hepes (pH 7.4), 150 mM NaCl, 5 mM $CaCl_2$, and 0.005% Tween-20. Initial velocities of the increase in fluorescence were determined for the enzymatic activity, and the relative activities of the mutants were calculated from a calibration curve for serially diluted wild-type ADAMTS13-MDTCS. The activity for each mutant was determined in duplicate or triplicate experiments.

ACKNOWLEDGMENTS. We thank M. Tomisako for her help in the crystallization, Y. Ben Ammar and the SPring-8 beamline staff for assistance with data acquisition, and D. Ginsburg (University of Michigan) for helpful comments on the manuscript. This work was supported, in part, by grants-in-aid from the Ministry of Health, Labor and Welfare of Japan, the Ministry of Education, Culture, Sports, Science and Technology of Japan, the Program for Promotion of Fundamental Studies in Health Sciences of the National Institute of Biomedical Innovation (NIBIO) of Japan, and the Takeda Science Foundation.

1. Porter S, Clark IM, Kevorkian L, Edwards DR (2005) The ADAMTS metalloproteinases. *Biochem J* 386:15–27.
2. Edwards DR, Handsley MM, Pennington CJ (2009) The ADAM metalloproteinases. *Mol Aspects Med* 29:258–289.
3. Sadler JE (1998) Biochemistry and genetics of von Willebrand factor. *Annu Rev Biochem* 67:395–424.
4. Ruggeri ZM (2003) Von Willebrand factor, platelets and endothelial cell interactions. *J Thromb Haemost* 1:1335–1342.
5. Sadler JE, Moake JL, Miyata T, George JN (2004) Recent advances in thrombotic thrombocytopenic purpura. *Hematology Am Soc Hematol Educ Program*, 407–423.
6. Dent JA, Berkowitz SD, Ware J, Kasper CK, Ruggeri ZM (1990) Identification of a cleavage site directing the immunochemical detection of molecular abnormalities in type IIA von Willebrand factor. *Proc Natl Acad Sci USA* 87:6306–6310.
7. Tsai HM, Sussman II, Nagel RL (1994) Shear stress enhances the proteolysis of von Willebrand factor in normal plasma. *Blood* 83:2171–2179.
8. Moake JL, et al. (1982) Unusually large plasma factor VIII:von Willebrand factor multimers in chronic relapsing thrombotic thrombocytopenic purpura. *N Engl J Med* 307:1432–1435.
9. Furlan M, et al. (1998) von Willebrand factor-cleaving protease in thrombotic thrombocytopenic purpura and the hemolytic-uremic syndrome. *N Engl J Med* 339:1578–1584.
10. Tsai HM, Lian EC (1998) Antibodies to von Willebrand factor-cleaving protease in acute thrombotic thrombocytopenic purpura. *N Engl J Med* 339:1585–1594.
11. Levy GG, et al. (2001) Mutations in a member of the ADAMTS gene family cause thrombotic thrombocytopenic purpura. *Nature* 413:488–494.
12. Soejima K, et al. (2001) A novel human metalloprotease synthesized in the liver and secreted into the blood: Possibly, the von Willebrand factor-cleaving protease? *J Biochem* 130:475–480.
13. Zheng X, et al. (2001) Structure of von Willebrand factor-cleaving protease (ADAMTS13), a metalloprotease involved in thrombotic thrombocytopenic purpura. *J Biol Chem* 276:41059–41063.
14. Soejima K, et al. (2003) ADAMTS-13 cysteine-rich/spacer domains are functionally essential for von Willebrand factor cleavage. *Blood* 102:3232–3237.
15. Zheng X, Nishio K, Majerus EM, Sadler JE (2003) Cleavage of von Willebrand factor requires the spacer domain of the metalloprotease ADAMTS13. *J Biol Chem* 278:30136–30141.
16. Ai J, Smith P, Wang S, Zhang P, Zheng XL (2005) The proximal carboxyl-terminal domains of ADAMTS13 determine substrate specificity and are all required for cleavage of von Willebrand factor. *J Biol Chem* 280:29428–29434.
17. Gao W, Anderson PJ, Sadler JE (2008) Extensive contacts between ADAMTS13 exosites and von Willebrand factor domain A2 contribute to substrate specificity. *Blood* 112:1713–1719.
18. Klaus C, et al. (2004) Epitope mapping of ADAMTS13 autoantibodies in acquired thrombotic thrombocytopenic purpura. *Blood* 103:4514–4519.
19. Luken BM, et al. (2005) The spacer domain of ADAMTS13 contains a major binding site for antibodies in patients with thrombotic thrombocytopenic purpura. *Thromb Haemost* 93:267–274.
20. Gerhardt S, et al. (2007) Crystal structures of human ADAMTS-1 reveal a conserved catalytic domain and a disintegrin-like domain with a fold homologous to cysteine-rich domains. *J Mol Biol* 373:891–902.
21. Mosyak L, et al. (2008) Crystal structures of the two major aggrecan degrading enzymes, ADAMTS4 and ADAMTS5. *Protein Sci* 17:16–21.
22. Takeda S (2009) Three-dimensional domain architecture of the ADAM family proteinases. *Semin Cell* Dev Biol 20:146–152.
23. Tan K, et al. (2002) Crystal structure of the TSP-1 type 1 repeats: A novel layered fold and its biological implication. *J Cell Biol* 159:373–382.
24. Takeda S, Igarashi T, Mori H, Araki S (2006) Crystal structures of VAP1 reveal ADAMs' MDC domain architecture and its unique C-shaped scaffold. *EMBO J* 25:2388–2396.
25. Kokame K, Nobe Y, Kokubo Y, Okayama A, Miyata T (2005) FRETS-VWF73, a first fluorogenic substrate for ADAMTS13 assay. *Br J Haematol* 129:93–100.
26. Zanardelli S, et al. (2006) ADAMTS13 substrate recognition of von Willebrand factor A2 domain. *J Biol Chem* 281:1555–1563.
27. de Groot R, Bardhan A, Ramroop N, Lane DA, Crawley JT (2009) Essential role of the disintegrin-like domain in ADAMTS13 function. *Blood* 113:5609–5616.
28. Zhang Q, et al. (2009) Structural specializations of A2, a force-sensing domain in the ultralarge vascular protein von Willebrand factor. *Proc Natl Acad Sci USA* 106:9226–9231.
29. Furlan M, Robles R, Lämmle B (1996) Partial purification and characterization of a protease from human plasma cleaving von Willebrand factor to fragments produced by in vivo proteolysis. *Blood* 87:4223–4234.
30. Tsai HM (1996) Physiologic cleavage of von Willebrand factor by a plasma protease is dependent on its conformation and requires calcium ion. *Blood* 87:4235–4244.
31. Kokame K, Matsumoto M, Fujimura Y, Miyata T (2004) VWF73, a region from D1596 to R1668 of von Willebrand factor, provides a minimal substrate for ADAMTS-13. *Blood* 103:607–612.
32. Luken BM, et al. (2006) Amino acid regions 572–579 and 657–666 of the spacer domain of ADAMTS13 provide a common antigenic core required for binding of antibodies in patients with acquired TTP. *Thromb Haemost* 96:295–301.
33. Gao W, Anderson PJ, Majerus EM, Tuley EA, Sadler JE (2006) Exosite interactions contribute to tension-induced cleavage of von Willebrand factor by the antithrombotic ADAMTS13 metalloprotease. *Proc Natl Acad Sci USA* 103:19099–19104.
34. Wu JJ, Fujikawa K, McMullen BA, Chung DW (2006) Characterization of a core binding site for ADAMTS-13 in the A2 domain of von Willebrand factor. *Proc Natl Acad Sci USA* 103:18470–18474.
35. Tortorella M, et al. (2000) The thrombospondin motif of aggrecanase-1 (ADAMTS-4) is critical for aggrecan substrate recognition and cleavage. *J Biol Chem* 275:25791–25797.
36. Kashiwagi M, et al. (2004) Altered proteolytic activities of ADAMTS-4 expressed by C-terminal processing. *J Biol Chem* 279:10109–10119.
37. Gendron C, et al. (2007) Proteolytic activities of human ADAMTS-5: Comparative studies with ADAMTS-4. *J Biol Chem* 282:18294–18306.
38. Flannery CR, et al. (2002) Autocatalytic cleavage of ADAMTS-4 (Aggrecanase-1) reveals multiple glycosaminoglycan-binding sites. *J Biol Chem* 277:42775–42780.
39. Fushimi K, Troeberg L, Nakamura H, Lim NH, Nagase H (2008) Functional differences of the catalytic and non-catalytic domains in human ADAMTS-4 and ADAMTS-5 in aggrecanolytic activity. *J Biol Chem* 283:6706–6716.
40. Kokame K, et al. (2002) Mutations and common polymorphisms in ADAMTS13 gene responsible for von Willebrand factor-cleaving protease activity. *Proc Natl Acad Sci USA* 99:11902–11907.
41. Banno F, Miyata T (2008) in *Recent Advances in Thrombosis and Hemostasis 2008*, eds Tanaka K, Davie EW (Springer, Tokyo), pp 162–176.
42. Akiyama M, Kokame K, Miyata T (2008) ADAMTS13 P475S polymorphism causes a lowered enzymatic activity and urea lability in vitro. *J Thromb Haemost* 6:1830–1832.
43. Plaimauer B, et al. (2006) Modulation of ADAMTS13 secretion and specific activity by a combination of common amino acid polymorphisms and a missense mutation. *Blood* 107:118–125.
44. Akiyama M, Takeda S, Kokame K, Takagi J, Miyata T (2009) Production, crystallization and preliminary crystallographic analysis of exosite-containing fragment of human von Willebrand factor-cleaving proteinase, ADAMTS13. *Acta Crystallograph Sect F Struct Biol Cryst Commun F* 65:739–742.

Acta Crystallographica Section F
Structural Biology and Crystallization Communications
ISSN 1744-3091

Masashi Akiyama,[a] Soichi Takeda,[a] Koichi Kokame,[a] Junichi Takagi[b] and Toshiyuki Miyata[a]*

[a]National Cardiovascular Center Research Institute, 5-7-1 Fujishirodai, Suita, Osaka 565-8565, Japan, and [b]Laboratory of Protein Synthesis and Expression, Institute for Protein Research, Osaka University, 3-2 Yamadaoka, Suita, Osaka 565-0871, Japan

Correspondence e-mail: miyata@ri.ncvc.go.jp

Received 17 April 2009
Accepted 18 June 2009

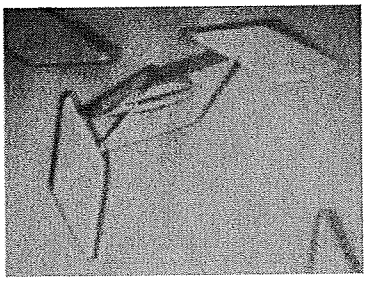

Production, crystallization and preliminary crystallographic analysis of an exosite-containing fragment of human von Willebrand factor-cleaving proteinase ADAMTS13

ADAMTS13 is a reprolysin-type metalloproteinase belonging to the ADAMTS (a disintegrin and metalloproteinase with thrombospondin type 1 motif) family. It specifically cleaves plasma von Willebrand factor (VWF) and regulates platelet adhesion and aggregation. ADAMTS13 is a multi-domain enzyme. In addition to the N-terminal metalloproteinase domain, the ancillary domains, including a disintegrin-like domain, a thrombospondin-1 type 1 repeat, a Cys-rich domain and a spacer domain, are required for VWF recognition and cleavage. In the present study, a fragment of the ADAMTS13 ancillary domains (ADAMTS13-DTCS; residues 287–685) was expressed using CHO Lec cells, purified and crystallized. Diffraction data sets were collected using the SPring-8 beamline. Two ADAMTS13-DTCS crystals with distinct unit-cell parameters generated data sets to 2.6 and 2.8 Å resolution, respectively.

1. Introduction

von Willebrand factor (VWF) is a plasma glycoprotein that is involved in platelet-dependent haemostasis (Sadler, 1998). VWF is primarily synthesized in vascular endothelial cells and megakaryocytes and is released into the plasma as ultralarge multimeric forms (UL-VWF) that are highly active in platelet adhesion and aggregation. A plasma metalloproteinase, ADAMTS13, specifically cleaves the Tyr1605-Met1606 peptidyl bond within the A2 domain of VWF (Dent *et al.*, 1990). Cleavage of UL-VWF into smaller forms by ADAMTS13 limits platelet thrombus formation. A deficiency of ADAMTS13 enzymatic activity caused by either genetic mutations in the ADAMTS13 gene or acquired autoantibodies against ADAMTS13 results in the accumulation of UL-VWF in plasma. This leads to the formation of disseminated platelet-rich microthrombi in arterioles, which is one of the characteristic pathogenic features of thrombotic thrombocytopaenic purpura (TTP), a life-threatening systemic disease (Tsai, 2009). Conversely, excessive cleavage of VWF causes von Willebrand disease type 2A (Sadler, 2005).

Human ADAMTS13 consists of 1427 amino acids and has a modular structure comprising a signal peptide, a short propeptide, a metalloproteinase domain (M), a disintegrin-like domain (D), a thrombospondin-1 type 1 repeat (T1), a Cys-rich domain (C), a spacer domain (S), seven additional type 1 repeats (T2–T8) and two CUB (C1r/C1s, urinary epidermal growth factor, bone morphogenic protein) domains (Levy *et al.*, 2001; Soejima *et al.*, 2001; Zheng *et al.*, 2001). C-terminal truncation of ADAMTS13 after the C but not the S domain results in severe loss of proteolytic activity towards VWF (Soejima *et al.*, 2003; Zheng *et al.*, 2003). Therefore, in addition to the M domain, the ancillary domains including the D, T, C and S domains (DTCS) are necessary for normal ADAMTS13 activity, although the distal C-terminal domains are required for regulation of *in vivo* thrombus formation under high-shear conditions (Banno et al., 2009). We have previously reported a minimal functional substrate consisting of 73 amino-acid residues of the C-terminal region of the VWF A2 domain (Asp1596–Arg1668) and designated VWF73 (Kokame *et al.*, 2004; Miyata *et al.*, 2007). A recent study has shown that the VWF-binding exosites located in the T, C and S domains interact with different segments of VWF73 (Gao *et al.*, 2008). These interactions increased the VWF-binding affinity and rate of substrate cleavage by

doi:10.1107/S1744309109023410

300-fold. At least 16 causative missense mutations for congenital TTP and five missense polymorphisms in the ADAMTS13 gene have been identified within the DTCS region (Levy *et al.*, 2001; Kokame *et al.*, 2002; Banno & Miyata, 2008). Although most TTP-causative mutant proteins are likely to show secretion deficiency, a P475S polymorphism variant showed normal secretion but reduced VWF-cleaving activity (Kokame *et al.*, 2002; Akiyama *et al.*, 2008). Detailed structural information on exosite-containing domains will help in understanding the structure-based mechanism of substrate recognition and specificity and the effects of TTP-causative mutations and common polymorphisms. To date, crystal structures of the M and D domains of three human ADAMTS-family proteins, ADAMTS1, ADAMTS4 and ADAMTS5, have been reported (Gerhardt *et al.*, 2007; Mosyak *et al.*, 2008; Shieh *et al.*, 2008). However, no crystal structures of exosite-containing fragments of ADAMTSs have been reported.

Here, we report the expression and purification of the exosite-containing human ADAMTS13-DTCS fragment using mammalian CHO Lec cells with mutations in multiple glycosylation-related genes. Proteins obtained from this cell line are suitable for crystallization because their restricted and homogeneous glycosylation improves the packing of the protein molecules. We also report the results of our crystallization and preliminary X-ray studies of ADAMTS13-DTCS.

2. Methods

2.1. Expression and purification of ADAMTS13-DTCS

An ADAMTS13 cDNA (AB069698) fragment corresponding to amino-acid residues 287–685 (ADAMTS13-DTCS) was amplified by PCR and cloned into a mammalian expression vector based on pcDNA3.1/Myc-His (Invitrogen), which has a mouse *Nid1* signal sequence (Yasui *et al.*, 2007). The nucleotide sequence was confirmed by dye-terminator sequencing. The ADAMTS13-DTCS fragment expressed from this vector contains a tobacco etch virus (TEV) proteinase cleavage site (Glu-Asn-Leu-Tyr-Phe-Gln/Gly) followed by tandem His-tag sequences at the C-terminus. We transfected the plasmid into CHO Lec 3.2.8.1 cells (Stanley, 1989) by electroporation and selected colonies resistant to G418 (3 mg ml^{-1}) on 96-well plates in α-minimal essential medium supplemented with 5% foetal bovine serum for 10 d. ADAMTS13-DTCS levels in the media of 48 G418-resistant colonies were examined by Western blotting with anti-6×His antibody (Sigma–Aldrich, St Louis, Missouri, USA). The clone with the highest secretion level of ADAMTS13-DTCS was cultured in the medium containing 0.5 mg ml^{-1} G418 by the roller-bottle method and the medium was collected every 3 d. The ADAMTS13-DTCS was recovered from the culture medium by 50%(*w*/*v*) ammonium sulfate precipitation and was purified by Ni–NTA agarose chromatography (Sigma–Aldrich). The eluted ADAMTS13-DTCS was incubated with TEV proteinase for 12 h at 297 K to remove the C-terminal tags. After dialysis in a buffer consisting of 10 m*M* MES and 100 m*M* NaCl pH 6.0, the digest was applied onto a Hi-Trap SP HP cation-exchange column (GE Healthcare, Buckinghamshire, England). The column was washed with the same buffer and ADAMTS13-DTCS was eluted with a linear gradient of NaCl (0.1–0.7 *M*) in 10 m*M* MES pH 6.0. Fractions were analyzed by SDS–PAGE under reducing conditions (Fig. 1). The fractions rich in ADAMTS13-DTCS (lanes 5 and 6) were combined, dialyzed against 10 m*M* MES pH 6.0 and concentrated using a Vivaspin-5 separation device (30 kDa molecular-weight cutoff; Sartorius, Edgewood, New York, USA) to a final concentration of ~10 mg ml^{-1} for crystallization.

2.2. Crystallization screening

Initial screening for crystallization conditions for ADAMTS-DTCS was carried out by the sitting-drop vapour-diffusion method using Index Screen, SaltRx Screen, PEG/Ion Screen, Grid Screen MPD and Grid Screen Ammonium Sulfate kits (Hampton Research, Aliso Viejo, California, USA). A volume of 0.1 µl protein solution was manually mixed with an equal amount of reservoir solution and the droplets were allowed to equilibrate against 0.1 ml reservoir solution at 293 K for 24 h.

2.3. Diffraction data collection

For X-ray measurements, crystals were soaked in a solution containing 20% glycerol, 26% PEG 1500, 100 m*M* MES pH 6.0 for cryoprotection prior to flash-freezing and were immediately exposed to a stream of nitrogen gas at 100 K. Preliminary X-ray data were collected using an in-house X-ray diffractometer (Micromax-007 X-ray generator with an R-AXIS VII imaging-plate detector; Rigaku, Tokyo, Japan) and diffraction-quality crystals were selected for data acquisition using the SPring-8 beamline. All the diffraction data sets were collected on beamline BL41XU at 100 K using an ADSC Quantum 310R detector and the diffraction images were processed using *HKL*-2000 software (Minor *et al.*, 2006).

3. Results and discussion

3.1. Protein preparation

We first attempted to express ADAMTS13-DTCS in *Escherichia coli* and insect cells. The expressed ADAMTS13-DTCS formed inclusion bodies and renaturation of ADAMTS13-DTCS did not succeed. We then tried to express ADAMTS13-DTCS in mammalian cells. As ADAMTS13-DTCS contains four potential N-glycosylation sites, we used the CHO Lec 3.2.8.1 cell line for stable expression. This cell line has four different mutated genes that are involved in the N- and O-glycosylation pathways (Stanley, 1989). Preliminary experiments showed that the endogenous signal and propeptide sequences of ADAMTS13 resulted in low protein secretion. We replaced the

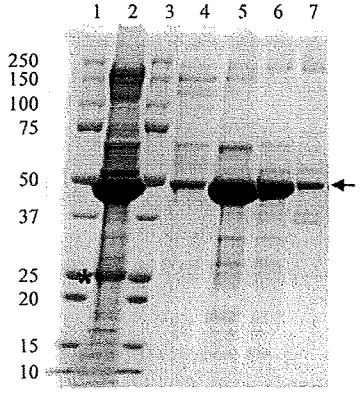

Figure 1
SDS–PAGE analysis of ADAMTS13-DTCS fractions from Hi-Trap SP HP cation chromatography. Proteins were analyzed by SDS–PAGE and stained with Coomassie Brilliant Blue. Lanes 1 and 3, molecular-weight markers (kDa); lane 2, pooled Ni–NTA eluate treated with TEV proteinase; lanes 4–7, eluate fractions Nos. 5–8, respectively, from the Hi-Trap SP HP column. Arrow, ADAMTS13-DTCS. Asterisk, TEV proteinase.

signal sequence and prosequence with the mouse *Nid1* signal sequence (Mann *et al.*, 1989). This replacement dramatically increased the secretion of ADAMTS13-DTCS into the medium. ADAMTS13-DTCS was purified by Ni–NTA chromatography followed by Hi-Trap SP cation-exchange chromatography. The molecular weight of the recombinant protein, 45 kDa, estimated by SDS–PAGE coincided well with the estimated molecular weight of 46 kDa (Fig. 1). Fractions (Fig. 1, lanes 5 and 6) from the Hi-Trap SP column were combined and used for crystallization without further purification. Approximately 6 mg ADAMTS13-DTCS was recovered from 20 l culture medium.

3.2. Crystallization

Of the 288 initial crystallization conditions tested, 20 yielded microcrystals (Fig. 2*a*). Using solution No. 4 of the PEG/Ion Screen kit [0.2 *M* lithium chloride, 20%(*w*/*v*) PEG 3350 pH 6.8] as a starting condition, the pH of the mother liquor, the concentration and molecular weight of the PEG and the species and concentrations of salts and additives were optimized. The combination of refinement of the crystallization conditions and an increase in the protein concentration (to ~20 mg ml^{-1}) improved the size of the crystals. Single crystals were obtained from drops made up of 0.5 µl protein solution and 0.5 µl reservoir solution [26%(*w*/*v*) PEG 1500, 100 m*M* MES pH 6.0] supplemented with a one-fifth volume of 40%(*w*/*w*) pentaerythritol ethoxylate (3/4 EO/OH; Additive Screen solution No. 52; Hampton Research). Crystals with dimensions of 300 × 100 × 50 µm were formed after 3–7 d at 293 K (Fig. 2*b*).

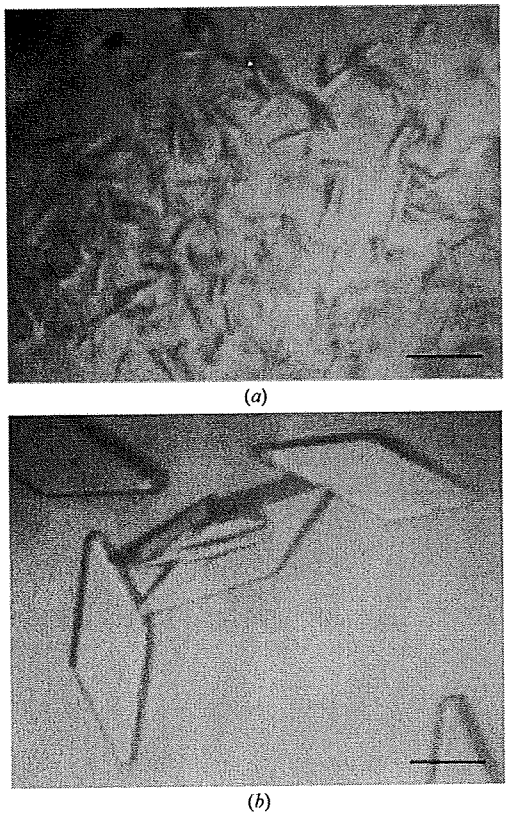

(*a*)

(*b*)

Figure 2
Crystals of human ADAMTS13-DTCS grown by the sitting-drop method. (*a*) Microcrystals obtained from solution No. 4 of the PEG/Ion Screen kit. (*b*) Crystals obtained using the optimized conditions. The scale bars indicate 0.1 mm.

Table 1
Data-collection statistics for ADAMTS13-DTCS crystals.

Values in parentheses are for the highest resolution shell. A single crystal was used for measurement for each data set.

	Form 1	Form 2
Space group	*C*2	*C*2
Unit-cell parameters		
a (Å)	152.7	138.6
b (Å)	52.9	51.4
c (Å)	76.2	76.4
β (°)	111.4	106.7
Wavelength (Å)	1.0	1.0
Resolution (Å)	50–2.60 (2.69–2.60)	30–2.80 (2.90–2.80)
No. of unique reflections	16867 (1272)	12811 (1259)
R_{merge}†	0.052 (0.176)	0.062 (0.403)
$I/\sigma(I)$	19.3 (5.7)	13.3 (3.5)
Completeness (%)	95.3 (72.7)	99.5 (99.3)
Redundancy	3.5 (2.9)	3.7 (3.6)
Matthews value (Å^3 Da^{-1})	2.64	2.39
Solvent content (%)	53.4	48.6

† $R_{merge} = \sum_{hkl}\sum_i |I_i(hkl) - \langle I(hkl)\rangle| / \sum_{hkl}\sum_i I_i(hkl)$, where $I_i(hkl)$ is the *i*th intensity measurement of reflection *hkl* and $\langle I(hkl)\rangle$ is its weighted average.

3.3. X-ray analysis

All diffraction data sets were acquired using the oscillation method on beamline BL41XU at a wavelength of 1.0 Å. The oscillation angle was 1.0° for all data sets. The native data sets for form 1 and form 2 contained 16 867 (2.60 Å resolution) and 12 811 (2.80 Å resolution) unique reflections, respectively. The asymmetric unit was estimated to contain one molecule, with corresponding crystal volume per protein weights of 2.7 and 3.1 Å^3 Da^{-1} for crystal forms 1 and 2, respectively. Solvent-content estimations based on a single copy of the molecule per asymmetric unit gave values of 53.4% and 48.6% for crystal forms 1 and 2, respectively. The X-ray data showed that the two crystal forms have different unit-cell parameters even when they are obtained under identical conditions. The variation in crystal packing might reflect the mobility of the domains in ADAMTS13-DTCS. The statistics of the data sets are summarized in Table 1.

3.4. Screening of heavy-atom derivatives

We attempted experimental phasing using heavy-atom derivatives because molecular replacement was not an option owing to the lack of related structures. The limited availability of single large crystals owing to the small amount of ADAMTS13-DTCS and its tendency to form multiple crystals produced difficulties in the search for heavy-atom derivatives. Therefore, we focused on investigating the colouring of crystals on heavy-atom soaking, which can be a good indication of heavy-atom binding. We selected 13 coloured compounds (Au-6, M1-10, M-11, M1-14, M1-15, M1-16, M1-17, M2-2, M2-3, M2-5, M2-16, M2-17 and M2-18) from Heavy Atom Screens (Hampton Research) and soaked small crystals in reservoir solution supplemented with each of these compounds. After several hours, we found that three osmium-containing compounds, ammonium hexabromoosmate (M2-16), potassium hexachloroosmate (M2-17) and osmium chloride (M2-18), were heavily absorbed into the crystals. To examine the X-ray diffraction from these potential derivatives, we prepared larger single crystals. We checked these using the in-house X-ray facility and well diffracting crystals were shipped for data acquisition at SPring-8. Structural analysis is now in progress using data obtained from the derivative soaked in the osmium chloride solution.

We thank M. Tomisako for her help with the crystallization experiments and Y. Ben Ammar and the staff of the SPring-8 beamline for assistance with the data acquisition. This work was supported in part by grants-in-aid from the Ministry of Health, Labour and Welfare of Japan, grants-in-aid from the Ministry of Education, Culture, Sports, Science and Technology of Japan, the Program for the Promotion of Fundamental Studies in Health Sciences of the National Institute of Biomedical Innovation (NIBIO) of Japan and a grant from the Takeda Science Foundation.

References

Akiyama, M., Kokame, K. & Miyata, T. (2008). *J. Thromb. Haemost.* **6**, 1830–1832.
Banno, F., Chauhan, A. K., Kokame, K., Yang, J., Miyata, S., Wagner, D. D. & Miyata, T. (2009). *Blood*, **113**, 5323–5329.
Banno, F. & Miyata, T. (2008). *Recent Advances in Thrombosis and Hemostasis*, edited by K. Tanaka & E. W. Davie, pp. 162–176. Tokyo: Springer.
Dent, J. A., Berkowitz, S. D., Ware, J., Kasper, C. K. & Ruggeri, Z. M. (1990). *Proc. Natl Acad. Sci. USA*, **87**, 6306–6310.
Gao, W., Anderson, P. J. & Sadler, J. E. (2008). *Blood*, **112**, 1713–1719.
Gerhardt, S., Hassall, G., Hawtin, P., McCall, E., Flavell, L., Minshull, C., Hargreaves, D., Ting, A., Pauptit, R. A., Parker, A. E. & Abbott, W. M. (2007). *J. Mol. Biol.* **373**, 891–902.
Kokame, K., Matsumoto, M., Fujimura, Y. & Miyata, T. (2004). *Blood*, **103**, 607–612.
Kokame, K., Matsumoto, M., Soejima, K., Yagi, H., Ishizashi, H., Funato, M., Tamai, H., Konno, M., Kamide, K., Kawano, Y., Miyata, T. & Fujimura, Y. (2002). *Proc. Natl Acad. Sci. USA*, **99**, 11902–11907.
Levy, G. G. *et al.* (2001). *Nature (London)*, **413**, 488–494.
Mann, K., Deutzmann, R., Aumailley, M., Timpl, R., Raimondi, L., Yamada, Y., Pan, T. C., Conway, D. & Chu, M. L. (1989). *EMBO J.* **8**, 65–72.
Minor, W., Cymborowski, M., Otwinowski, Z. & Chruszcz, M. (2006). *Acta Cryst.* D**62**, 859–866.
Miyata, T., Kokame, K., Banno, F., Shin, Y. & Akiyama, M. (2007). *Curr. Opin. Hematol.* **14**, 277–283.
Mosyak, L. *et al.* (2008). *Protein Sci.* **17**, 16–21.
Sadler, J. E. (1998). *Annu. Rev. Biochem.* **67**, 395–424.
Sadler, J. E. (2005). *Annu. Rev. Med.* **56**, 173–191.
Shieh, H. S., Mathis, K. J., Williams, J. M., Hills, R. L., Wiese, J. F., Benson, T. E., Kiefer, J. R., Marino, M. H., Carroll, J. N., Leone, J. W., Malfait, A. M., Arner, E. C., Tortorella, M. D. & Tomasselli, A. (2008). *J. Biol. Chem.* **283**, 1501–1507.
Soejima, K., Matsumoto, M., Kokame, K., Yagi, H., Ishizashi, H., Maeda, H., Nozaki, C., Miyata, T., Fujimura, Y. & Nakagaki, T. (2003). *Blood*, **102**, 3232–3237.
Soejima, K., Mimura, N., Hirashima, M., Maeda, H., Hamamoto, T., Nakagaki, T. & Nozaki, C. (2001). *J. Biochem.* **130**, 475–480.
Stanley, P. (1989). *Mol. Cell. Biol.* **9**, 377–383.
Tsai, H. M. (2009). *Kidney Int. Suppl.*, pp. S11–S14.
Yasui, N., Nogi, T., Kitao, T., Nakano, Y., Hattori, M. & Takagi, J. (2007). *Proc. Natl Acad. Sci. USA*, **104**, 9988–9993.
Zheng, X., Chung, D., Takayama, T. K., Majerus, E. M., Sadler, J. E. & Fujikawa, K. (2001). *J. Biol. Chem.* **276**, 41059–41063.
Zheng, X., Nishio, K., Majerus, E. M. & Sadler, J. E. (2003). *J. Biol. Chem.* **278**, 30136–30141.

Nuclear Instruments and Methods in Physics Research A 608 (2009) S7–S10

Contents lists available at ScienceDirect

Nuclear Instruments and Methods in Physics Research A

journal homepage: www.elsevier.com/locate/nima

A trial for fine and low-dose imaging of biological specimens using quasi-monochromatic laser-Compton X-rays

K. Yamada [a,*], R. Kuroda [a], H. Toyakawa [a], H. Ikeura-Sekiguchi [a], M. Yasumoto [a], M. Koike [a], F. Sakai [b], K. Mori [c], H. Mori [d,e], N. Fukuyama [e], E. Sato [f]

[a] National Institute of Advanced Industrial Science and Technology, Tsukuba, Japan
[b] Sumitomo Heavy Industries, Ltd., Nishi-Tokyo, Japan
[c] Ibaraki Prefectural University of Health Sciences, Inashiki, Japan
[d] National Cardiovascular Center, Suita, Japan
[e] Tokai University, School of Medicine, Isehara, Japan
[f] Iwate Medical University, Morioka, Japan

ARTICLE INFO

Available online 31 May 2009

Keywords:
Inverse-Compton scattering
Quasi-monochromatic X-ray
Refraction-contrast imaging
K-edge-contrast imaging

ABSTRACT

The laser-Compton X/gamma-rays produced through the inverse-Compton scattering process are acknowledged as excellent tools in basic science and industrial technologies. At the National Institute of Advanced Industrial Science and Technology (AIST), two Compton systems based on a compact S-band linac and a versatile storage ring are working in photon energy ranges of 10–40 keV and 1–40 MeV. Compton X-rays in the lower energy range are thought to be suitable to make the fine and low-dose imaging in biology or medicine due to their partial spatial coherence and quasi-monochromaticity. Here we report some typical examples for medical imaging by Compton X-rays using the phase-contrast and K-edge-contrast schemes. It will be also shown that a distinctive image was taken by a single-shot picosecond Compton X-ray pulse which will enable us not only to take a still-shot of dynamic behaviour in organs but also to achieve a real-time motion picture using successively obtained single-shot images.

1. Introduction

Advanced quantum-beam sources, such as laser-Compton X/gamma-rays [1,2], first-switching polarizing-undulator radiations [3], free-electron lasers [4], and pulsed slow-positron beams [5], are being developed at the National Institute of Advanced Industrial Science and Technology (AIST) accelerator facility. Laser-Compton X/gamma-rays are especially useful to investigate the inside of living bodies or structures composed of high-density materials non-destructively. Experiments to generate quasi-monochromatic gamma-rays through the inverse-Compton scattering process were started at AIST around 1984 by focusing high-power lasers onto high-energy electron beams in the storage ring named TERAS [6]. Due to the high photon energy (typically 1–40 MeV) obtained in this system, the laser-Compton gamma-rays have been used as excitation sources for photo-nuclear reactions [7] and also as powerful probes for three-dimensional non-destructive inspection [8] of industrial products including high-density materials. Another lower energy laser-Compton system based on a compact S-band linac and a high-power femtosecond laser system had also been developed in collaboration with Sumitomo Heavy Industries Ltd. in the National R&D program promoted by the New Energy and Industrial Technology Development Organization (NEDO) and was transferred to AIST in 2005. Recently lower energy Compton systems are being developed at several facilities [9–12]. The photon energy obtained in such systems is in an X-ray range of the order of 10 keV, which is favorable for biological research. In this article, a brief explanation of our Compton X-ray system and recent results of its application to medical imaging will be given.

2. Compton X-ray system at AIST

Fig. 1 shows the AIST Compton X-ray system based on an S-band compact linac and a high-power femtosecond Ti:Sa laser. The linac is composed of a laser-photocathode RF gun, two 1.5 m S-band accelerator tubes, an achromatic arc and beam-focusing optics. A Cu or Cs–Te photocathode is irradiated by the 4th harmonic of picosecond Nd:YLF lasers whose energy is about 100 or 10 μJ/pulse for the respective cathode materials, and a highly brilliant electron bunch of about 3 ps (rms) in duration and 1–2 nC in charge is emitted from the RF gun. The electron bunch is successively accelerated up to 40 MeV at the maximum with the

* Corresponding author.
E-mail address: k.yamada@aist.go.jp (K. Yamada).

0168-9002/$ - see front matter © 2009 Elsevier B.V. All rights reserved.
doi:10.1016/j.nima.2009.05.157

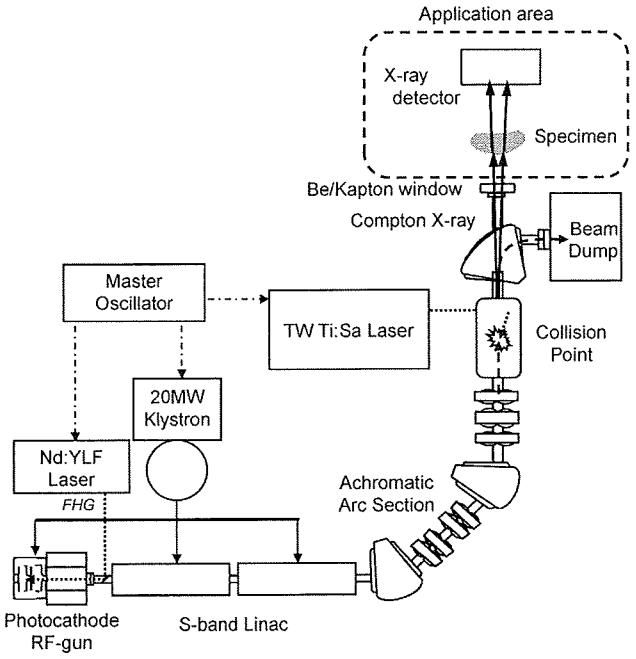

Fig. 1. Schematic view of the AIST Compton X-ray system.

S-band accelerator, and synchronously collided by 100 fs and 100 mJ Ti:Sa laser pulses at 10 pps after the achromatic arc section. In the inverse-Compton scattering process, photons with angular energy-distribution are scattered ahead of the electron-beam propagation direction. Quasi-monochromatic photons are usually extracted by passing only the central part of the photon beam through an appropriate aperture. The collision angle between electron beams and laser pulses determines the maximum energy and duration of scattered X-ray pulses: 20 keV and 150 fs for the side-on collision and 40 keV and 3 ps for the head-on collision. The number of photons in each X-ray pulse depends on the collision angle and the permitted photon energy spread. Since an energy spread of ~10% is acceptable in the imaging application, X-rays of the order of 10^6 photons/s are available on the object surface in the near head-on (165°) collision condition. After scattering the X-rays, the electron beam is dumped with a dipole magnet and the X-rays are transferred to the application area through a beryllium window.

3. Application of the Compton X-rays to the medical imaging technology

Compton X-rays have partial spatial coherence and quasi-monochromaticity in a moderate energy range available for biological observation. We applied such characteristics to the fine and low-dose imaging of biological specimens using refraction-contrast and K-edge-contrast schemes.

3.1. Refraction-contrast imaging

Refraction contrast is a kind of an in-line phase-contrast scheme. A simple explanation of this is given in Fig. 2. When an X-ray beam with spatial coherence is incident on an object including high- and low-density regions, it will be refracted around the boundary of the region due to some phase shift caused by deferent refractive indices in each region and the contrast in the image will be enhanced at an appropriate distance from the object even in almost transparent materials. Here, it should be noted that the refraction occurs in the reverse direction because the refractive indices are less than one for X-rays. So far, refraction-contrast scheme has been intensively studied using synchrotron radiation [13]. Effectiveness of this scheme was demonstrated also in the Compton X-ray imaging [14]. The specimen was set at 2.97 m from the Compton collision point (see Fig. 1) and the images were taken with an imaging plate at different distances from the specimen. In the refraction-contrast scheme, spatial coherence of X-rays is required as explained above. The small spot size of the Compton collision (~30 μm) seems to contribute to the partial spatial coherence of the Compton X-ray beams. Fig. 3 shows the typical images taken at the distances of 40 mm (a), 200 mm (b) and 750 mm (c) from the specimen. Here, the specimen was a lumbar vertebra of a rat and the X-ray energy was tuned to 30 keV. The traces are density scans for each rectangular area indicated in the above images. In this figure it is found that the image contrast between the bone and soft tissue in the lumbar vertebra becomes more distinctive with increasing distance, and the effect of refraction contrast is more important especially at the distance more than 200 mm. Since the Compton X-rays are generated at 2.97 m away from the specimen

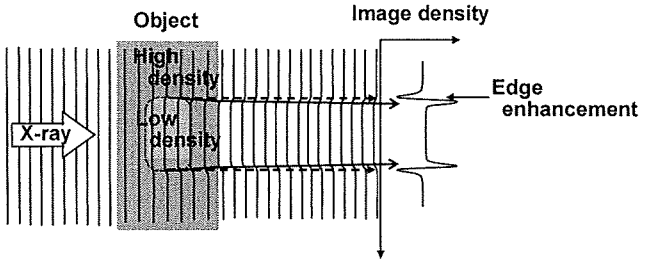

Fig. 2. Simple explanation of the refraction-contrast scheme.

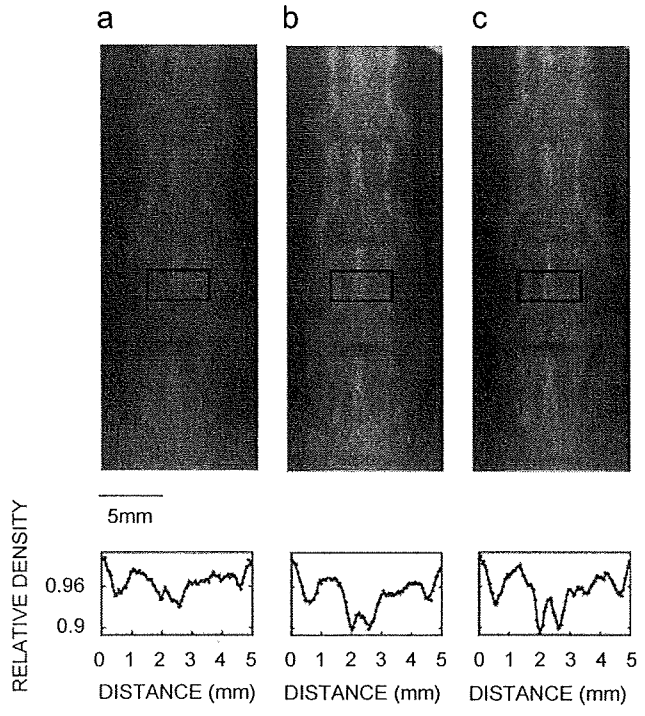

Fig. 3. Typical images taken at 40 mm (a), 200 mm (b) and 750 mm (c) from the lumbar vertebra of a rat.

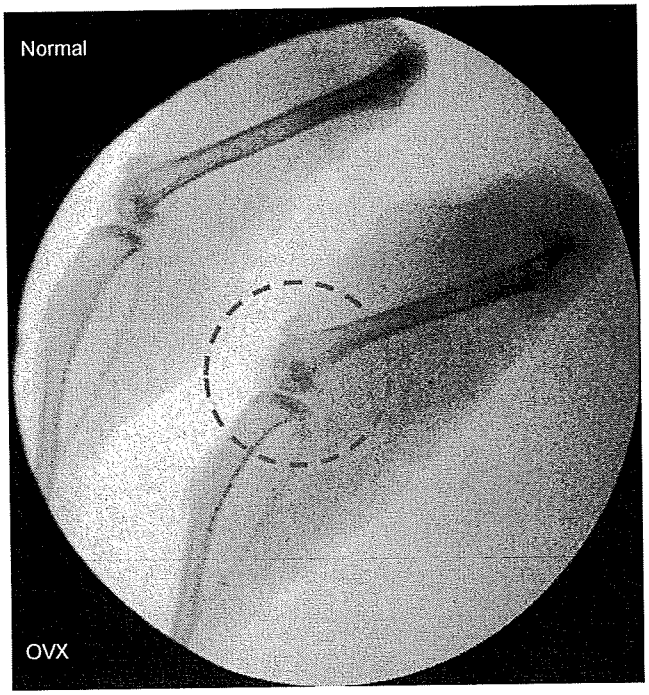

Fig. 4. X-ray image of hind limbs of normal mouse (upper) and ovariectomized (OVX) mouse (lower). Bone edge is observed to be obscure in the dashed circle which may indicate a symptom of the osteoporosis.

with a finite divergence angle, the magnification and the X-ray flux in each image were different. Therefore, they were compensated against the imaging distance in Fig. 3.

Fig. 4 shows another example of the Compton X-ray imaging. The specimens were hind limbs of a normal mouse and an ovariectomized (OVX) mouse which can suffer from osteoporosis. The X-ray energy was 26 keV in this observation. This image was obtained using an imaging plate at 200 mm behind the specimens where the refraction contrast is expected to be effective. In case of the OVX mouse, the osteoporosis may cause some sponge-like structure inside its bones. Actually, the bone edge around the knee joint is observed to be clear and tight in the normal mouse (upper image), while it is found to be obscure in the OVX mouse (lower image) as shown in the dashed circle. This suggests the occurrence of bone erosion, which may indicate a symptom of osteoporosis. Further inspection will be necessary to verify this argument.

To obtain images in Figs. 3 and 4, X-ray was accumulated for 30 min on the imaging plate. Since our Compton system is operated at 10 pps in the near head-on collision mode, 30 min contain 18,000 X-ray pulses of 3 ps in rms. In this case the effective time for the specimen to be exposed by the X-rays is only about 100 ns. Considering such a short exposure time as well as quasi-monochromaticity of the X-rays, the Compton X-ray-based refraction-contrast imaging can be a very useful scheme as a low-dose medical imaging technique.

3.2. *K-edge-contrast imaging*

Characteristic X-ray absorption by the K-edge of iodine is widely used in angiography for relatively thick blood vessels. In this case, a conventional X-ray tube is usually used as a simple and convenient irradiation source. Such a K-edge-contrast scheme was successfully applied to the micro-angiography in arterioles using synchrotron radiations as intense and monochromatic X-ray sources [15,16]. Compton X-ray is also expected to be an alternative irradiation source for fine and low-dose micro-angiography in clinic-scale due to its partial spatial coherence and quasi-monochromaticity as well as the compactness of the total system. We made a preliminary experiment to confirm this. The experimental setup was almost the same as that in the refraction-contrast scheme except that a different type of X-ray detector was placed just behind the specimen. In medical use, a real-time data acquisition becomes important, because some moving objects, such as a beating heart or thin blood vessels responding dynamically to physical conditions, often must be imaged. To meet this demand, a highly sensitive real-time camera based on a high-gain avalanche rushing photoconductor (HARP) [17] was adopted for an X-ray detector. The HARP camera has sensitivity higher than that of a CCD camera for high-definition recordings by at least one order of magnitude in the real-time mode and more than three orders of magnitude in the accumulation mode. Although the original sensing range of HARP is in the visible wavelength, it can be used even for the X-ray range by attaching an X-ray image intensifier (XII).

At first, we tried to take pictures of a resolution chart by Compton X-rays using this real-time imaging system in video-rate recording mode where the time interval between each frame is 33.3 ms. Since our Compton X-ray system is operated at 10 pps, time interval of the X-ray pulses is 100 ms, which means one frame in the video-rate recording can contain only one X-ray pulse. Fig. 5 shows one frame extracted from a video-rate motion picture. It is shown in Fig. 5 that a distinctive image with a spatial resolution of ~250 μm was observed. To our knowledge, this is the first success in imaging by a single picosecond Compton X-ray pulse. The spatial resolution was found to be improved to ~125 μm in 1-s accumulation mode of the HARP camera where the signal charges induced by ten X-ray pulses were accumulated to enhance the effective sensitivity. In this case an intermittent motion picture with one frame per second can be obtained. This Compton X-ray imaging system was applied to the micro-angiography of a biological specimen. Fig. 6 shows the angiographic image of a rabbit ear, vascular beds of which were filled with iodine-labelled microspheres with a diameter of 15 μm. In this observation, the Compton X-ray was tuned to ~33 keV, which was near the K-edge of iodine and the HARP camera was operated in 1-s accumulation mode. In Fig. 6, it is found that the 3rd vascular branch of 480 μm in bore is definitely observed. This is just a preliminary result of the real-time K-edge-contrast imaging by the Compton X-rays where various experimental parameters, such as the gain and accumulation time of HARP, tuning of imaging optics between the HARP, XII and X-ray energy,

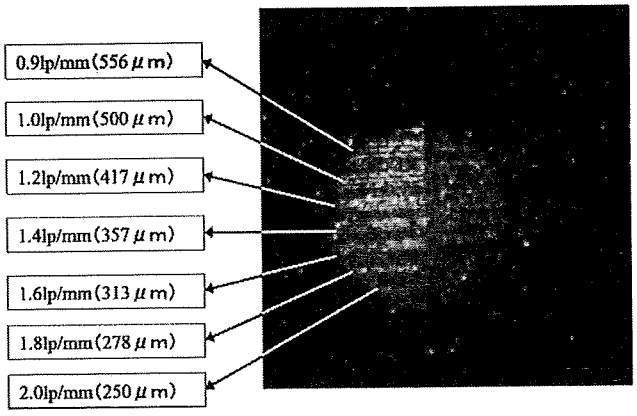

Fig. 5. An image of a resolution chart taken by a single picosecond Compton X-ray pulse.